
Article:
Tao, X., Liu, X., Matthews, A. et al. (1 more author) (2019) The influence of stacking fault energy on plasticity mechanisms in triode-plasma nitrided austenitic stainless steels: Implications for the structure and stability of nitrogen-expanded austenite. Acta Materialia, 164. pp. 60-75. ISSN 1359-6454

https://doi.org/10.1016/j.actamat.2018.10.019

The influence of stacking fault energy on plasticity mechanisms in triode-plasma nitrided austenitic stainless steels: implications for the structure and stability of nitrogen-expanded austenite.

Author: Xiao Tao[a], Xingguang Liu[a, c], Allan Matthews[b], Adrian Leyland[a]*

[a]Department of Materials Science and Engineering, The University of Sheffield, Sheffield, S1 3JD, United Kingdom

[b]School of Materials, The University of Manchester, Manchester, M13 9PL, United Kingdom

[c]National Key Laboratory of Science and Technology on Vacuum Technology and Physics, Lanzhou Institute of Physics, Lanzhou Gansu, 730010, China

Xiao Tao: xtao1@sheffield.ac.uk or hugou2008@hotmail.com
Xingguang Liu: xingguangliu1@gmail.com
Allan Matthews: allan.matthews@manchester.ac.uk

*Corresponding author: Dr. Adrian Leyland
Email: a.leyland@sheffield.ac.uk
Telephone: +44 (0) 114 222 5486,
Fax: +44 (0) 114 222 5943
Full postal address: Department of Materials Science and Engineering, Sir Robert Hadfield Building, Mappin Street, Sheffield, S1 3JD, United Kingdom

Abstract

Austenitic stainless steels (ASSs), especially AISI type 304 and 316 ASSs, have been extensively studied after thermochemical diffusion treatments (e.g. nitriding, carburising) to resolve the anomalous lattice expansion after supersaturation of interstitial elements under paraequilibium conditions. The known issues are i) plastic deformation of surfaces under nitrogen-introduced strain at low treatment temperatures and ii) degradation in surface corrosion performance in association with chromium nitride formation at elevated treatment temperatures (and/or longer treatment times). In this study, a nitrogen-containing high-manganese ASS and a high-nickel ASS (i.e. Fe-17Cr-20Mn-0.5N and Fe-19Cr-35Ni, in wt.%) were triode-plasma nitrided under a high nitrogen gas volume fraction and low (and close to monoenergetic) ion energy of ~200 eV at 400°C, 425°C and 450°C for 4hrs and 20hrs, respectively. Auxiliary radiant heating was used to facilitate different treatment temperatures at a deliberately controlled and constant substrate current density of ~0.13 mA/cm^2, under which material surface crystallographic structure was mainly influenced by the different treatment temperatures and times applied during nitriding. With respect to stacking fault energy (SFE), we illustrate and discuss i) the analogy of composition-induced plastic deformation phenomena to mechanical deformation processes, ii) two possible types of dislocation-mediated plasticity mechanism in γ_N, iii) two possible types of diffusional decomposition mechanism for γ_N, and iv) the lattice structures formed at low to moderate nitriding temperatures.

Key words: Austenitic stainless steels; Stacking-fault energy; Expanded austenite; X-ray diffraction (XRD); Electron diffraction pattern

1 Introduction

Low temperature thermochemical diffusion modification of austenitic stainless steel (ASS) was originally identified as an unanticipated corrosion induced carbon transportation mechanism – and thus a topic of interest (and of concern) − by the nuclear power industry in the early 1960s [1-6] but, as reviewed recently by Somers and Christiansen [7], was subsequently investigated systematically in the open literature from the 1980s as a potential solution to the poor tribological performance of ASS [8-24]. The unusual crystallographic structures observed after treatment, and the remarkable enhancement of surface mechanical/tribological properties that these structures provided (without loss of corrosion resistance), led to a drive to try to understand their origin. Over an approximately parallel timeframe to the above, systematic investigations at the Netherlands Organisation for Applied Scientific Research (TNO) during the 1970s by Kolster [6], on the transport of alloying elements of steels in liquid sodium cooling systems, led to the development of a successful proprietary low-temperature gaseous carburising treatment for ASSs from the 1980s (the so-called 'Hardcor' process of Hardcor B.V. − later renamed as 'Kolsterising®' by the subsequent owner Bodycote Plc. in recognition of the ground-breaking efforts by Kolster) [25-27]. In the scientific literature, the apparently mono-phased (but clearly crystallographically 'different') surface region generated after low temperature thermochemical treatment of stainless steels was initially referred to as 'S-phase' by Ichii et al. [9] in 1986, as 'm-phase' by Marchev et al. [15] in 1998, as 'γ_N' by Williamson et al. [10] in 1990 and, somewhat more precisely, as 'expanded austenite' by Leyland et al. [11] in 1993.

After decades of intellectual effort [12, 17, 20-22, 24], expanded austenite is now widely recognised (but still not totally understood) as a metastable, anisotropically expanded face-centred cubic (FCC) austenite (γ_C or γ_N, as respectively supersaturated with interstitial carbon or nitrogen), generated under 'paraequilibrium' conditions [28, 29], at low temperatures and (typically) over long timescales, far from thermodynamic equilibrium. During low temperature diffusion treatment of austenite, the diffusivities of small interstitial elements (i.e. C and N) are several orders of magnitude higher than those of the relatively 'immobile' substitutional elements (e.g. Fe, Cr, Ni and Mn) [12] − such that interstitial elements diffuse inward from the substrate surface, following a chemical potential gradient. The formation of thermodynamically-favoured carbides/nitrides is suppressed, owing to the low substitutional element diffusivity, whereas the interstitial element paraequilibium solubility in ASSs has been reported to be at least several hundred times higher than the equilibrium solubility during thermochemical treatment (e.g. up to ~19 at.% C and ~38 at.% N in AISI 316 after carburising at 380°C [30] and after nitriding at 420°C/445°C [21], respectively). Under conditions of paraequilibium, there is no crystallographic phase transformation of the modified (anisotropically expanded) austenitic lattice [18, 19, 23]; nevertheless, phase decomposition can occur eventually, with chromium nitride (and/or carbide) formation (either after prolonged treatment or at elevated temperature), which leads to Cr-depleted volumes at the material surface (and locally within grain boundary regions) − thereby deteriorating alloy corrosion resistance [28-32].

The crystallographic structure of expanded austenite, as determined from the hkl-dependent peak shifts and broadening in X-ray diffractograms, deviates from the ideal FCC structure. The anomalous anisotropic lattice expansion was attributed to the combined effect of two aspects in the FCC lattice: i) residual stress associated with the hkl-dependent planar elastic constants and ii) stacking fault (SF) generation associated with the hkl-dependent stacking fault parameters [17, 22, 24]. Together with the concentration gradient of interstitial species from surface to core for the expanded austenite layers formed on bulk materials by thermochemical diffusion, the two abovementioned interrelated aspects complicate scientific interpretation of observable XRD profiles for expanded austenite.

Moreover, lattice elasticity/plasticity has been increasingly discussed in recent literature [24, 33-36], where the elusive structure of γ_N might originate from 'plastic' deformation of austenite under N-interstitially introduced strain. Further to a transmission electron microscopic study by Tong et al. [37], TEM diffraction patterns of the high SF density regions in γ_N under nitrogen-interstitially introduced strain [18, 19, 37-39] appear strikingly similar to the SFs, deformation twinning and/or stress-induced hexagonal closed packed (HCP) ε-martensite seen in mechanically-deformed ASS [40], as illustrated (at the $[110]_{matrix}$ zone axis) in **Fig. 1**. That is, the nitrogen interstitially supersaturated FCC lattice could undergo plasticity mechanisms, such as generation of SFs on $\{111\}\gamma_N$ planes [18, 19], lattice twinning [38, 39], and/or martensitic shear transformation [37], similar to that of FCC alloys under mechanical deformation. The stacking fault energy (SFE) of austenite, which is, for example ~18 mJ/m^2 for AISI 304

[41, 42] − where both deformation twinning and/or martensitic transformation may occur under mechanical deformation − will directly influence the propensity of the strained lattice to undergo martensitic shear transformation, twinning, or dislocation-mediated slip (or combinations thereof). In this case, the SFE value of γ_N on the particular ASS substrate material being treated under low-temperature nitriding or carburising (and how this value changes with treatment time/temperature) must contribute significantly to the lattice structures formed.

As the most widely used ASS grades, types AISI 304 (i.e. Fe-18Cr-8Ni, in wt.%) and AISI 316 (i.e. Fe-18Cr-11Ni-3Mo, in wt.%) have both been studied extensively after nitriding (and/or carburising). ASSs are based fundamentally on a ternary system of Iron-Chromium-Nickel (Fe-Cr-Ni), where Ni can be replaced with Mn (wholly, or in part) for economic or other (e.g. biocompatibility, work-hardening propensity) reasons. Cr has been widely referred to in the literature as an 'essential' element in the formation of γ_N, believed to assist in 'trapping' of the inwardly-diffusing interstitial species and (in the case of nitrogen) forming short-range ordering of Cr-N [14, 23, 29, 43, 44]. However, the synergistic effects of Ni and Mn on the structural response (i.e. lattice expansion and/or phase decomposition) during thermochemical treatment with nitrogen and/or carbon are still unclear. In this study, two proprietary commercial alloys, ATI Staballoy AG17® (i.e. Fe-17Cr-20Mn-0.5N, in wt.%) and RA 330® (i.e. Fe-18Cr-35Ni, in wt.%), were selected for reasons of i) an equivalent Cr content (i.e. ~17-18 wt.%) without other strong nitride forming elements present and, ii) a high content of the

austenite-stabilising substitutional element (i.e. 20 wt.% Mn and 35 wt.% Ni, respectively). A range of experimental treatment parameters were chosen, such that both high lattice expansion (with apparent plastic deformation under N-introduced strain) and phase decomposition effects could be obtained in ASS alloys AG17 and 330 via the low-temperature triode-plasma nitriding (TPN) technique [11, 45].

Both substitutional (Ni, Mn) and interstitial (N, C) species will influence the SFE of ASSs; however, there is a lack of SFE data for the precise compositions of the AG17 and 330 proprietary alloys chosen for this work. From the literature, a higher Ni content clearly increases SFE (from ~17 mJ/m^2 at 8 at.% Ni to ~31 mJ/m^2 at 30 at.% Ni) in an Fe-Cr-Ni ternary system containing ~18-20 at.% Cr [46, 47]. Alloy 330 is thus likely to have a much higher SFE than 304 (probably in excess of 30 mJ/m^2) for this positive effect of Ni on SFE; in which case, planar dislocation glide tends to be promoted under strain. Furthermore, Gavriljuk et al. [48] measured experimentally a SFE of ~21 mJ/m^2 for an alloy of composition quite similar to AG17 (Fe-15Cr-17Mn-0.5N) – i.e. slightly higher than (but approximately equivalent to) AISI 304 (at ~18 mJ/m^2). However, based on a thermodynamic model for the Fe-Cr-Mn-N system developed by Mosecker et al. [49], the SFE of AG17 might lie between ~10-18 mJ/m^2 for the occurrence of twinning and/or martensitic transformation; i.e. values similar to (or perhaps somewhat lower than) those reported for AISI 304 [41, 42].

The SFE of ASSs can profoundly influence the structure and phase stability of expanded austenite under thermochemical treatment. Taking the available room temperature SFE data of two selected substrates as a reference, the SF number density in γ_N-AG17 (synthesised on relatively low SFE AG17 alloy under TPN) might be higher than that in γ_N-330 (synthesised on relatively high SFE alloy 330 under TPN). Additionally, Ernst et al. [29] indicated that decomposition of expanded austenite (γ_C in their study) requires i) a substantial lattice expansion, to reduce the volume-misfit stress for precipitation, and ii) a high density of lattice defects (e.g. SFs), to locally enhance substitutional segregation. The expected higher SF density in γ_N-AG17 might result in a lower thermodynamic structural stability under diffusion treatment, as compared to γ_N-330.

Ni and/or Mn content in ASSs will also influence the formation and decomposition of γ_N via factors other than SFE. Firstly, Ni addition to the substrate is thought to lower the equilibrium N solubility in austenite − and hence reduce N uptake during nitriding − whereas Mn addition is thought to increase it. For example, Williamson et al. [14] illustrated that austenitic Ni-based alloys possess lower surface N-absorption compared to austenitic Fe-based alloys. However, the effect of Ni content was not unambiguously demonstrated in ASSs, because the austenitic alloys in their study contained varying concentrations of Cr and/or significant amount of other nitride forming elements (e.g. Al, Ti and Mo to a few wt.%) [14]. Buhagiar et al. [50] showed that replacement of Ni with approximately the same mass content of Mn in ASSs enhanced nitrogen uptake in expanded austenite. For the decomposition of γ_N, substitutional diffusivity (i.e. the

migration speed of substitutional elements towards or away from precipitate 'embryos') is likely to be significantly influenced by alloy compositional factors (such as Ni/Mn content). For example, the formation of χ carbide in AISI 316 during low temperature carburising requires outward migration of Ni from the carbide 'embryo', where the relative low diffusivity of Ni under paraequilibrium conditions plays an important role in retarding carbide formation [29]. In contrast, Mn possesses a higher solid solution diffusivity than both Fe and Cr in the Fe-Cr-Mn system [51], in which case Mn_3N_2 precipitation was reported to favourably occur in γ_N for a Ni-free Mn-stabilised ASS after low temperature nitriding [50]. These two conventional aspects imply greater nitrogen solubility in (but lower phase stability of) the high-Mn γ_N-AG17, as compared to the high-Ni γ_N-330, in our present study.

Last but not least, the different substitutional contents of Mn/Ni, as the two major austenite-stabilising elements in commercial grades of ASS, will influence the decomposition mechanisms in a nitrogen-supersaturated FCC lattice by varying the ferrite-austenite transformation temperature. The decomposition mechanism of γ_N is known for AISI 304L to be $\gamma_N \rightarrow$ [α-ferrite + CrN], whereas for AISI 316L (having a higher Ni content than AISI 304L) $\gamma_N \rightarrow$ [γ-austenite + CrN] is commonly reported [52, 53]. Given the potentially high N-content in γ_N-AG17, the pre-existing N-content in the unmodified AG17 substrate appears to be a somewhat trivial factor in determining the dominant decomposition mechanism during thermochemical diffusion treatment.

2 Experimental

2.1 Materials investigated

Three commercial alloys: AISI 304, Staballoy AG17® (ATI Allvac Ltd.) and RA 330® (NeoNickel Ltd.) were prepared as 50×25×4 mm rectangular coupons. Sample compositions were examined using EDX and chemical analysis, with the results shown in **Table 1**. Each substrate coupon was mechanically ground and polished to a mirror finish (i.e. Ra ~ 0.02 μm) using Buehler MetaDi^{TM} monocrystalline diamond suspension in the final steps (6 μm to 1 μm, successively). The samples were cleaned ultrasonically in acetone for 15mins, in isopropanol for 10mins, and dried using dry compressed air.

2.2 Triode-plasma nitriding treatments

The polished sample coupons (and two 'dummy' stainless steel coupons of size ~50×25×4mm) were mounted on a stainless steel load stage inside a modified Tecvac IP70L vacuum chamber. A type-K thermocouple was inserted into each dummy sample for temperature monitoring and control. The average temperature was measured and maintained constant during the treatment process. Nitriding was performed using a modified d.c. plasma configuration (i.e. triode configuration [11, 45]), where an additional tungsten filament is used as a thermionic electron emitter to enhance ionisation of the treatment gas mixture during the process. Alloys AG17 and RA 330 were nitrided at 400°C, 425°C and 450°C for 4hrs and 20hrs, respectively − whilst alloy AISI 304 was nitrided at 450°C only, for comparison purposes.

The treatment chamber was firstly evacuated to a base pressure of 2×10^{-3} Pa. Substrate samples were then biased at -800V for 15 mins under an argon (Ar) partial pressure of 2 Pa for sputter cleaning. Auxiliary radiant heating was used together with plasma heating to raise (at a rate of ~7°C/min) − and then maintain − the treatment temperature. A gas mixture of Ar and N_2 (at an Ar:N_2 volumetric ratio of 3:7) was used at an ultra-low constant chamber pressure of 0.4 Pa during TPN (conventional diode plasma nitriding operates at much higher gas pressures − typically in the 0.1-1.0 kPa range). Sample coupons and the hot tungsten filament plasma-enhancement device were both biased at -200 V during TPN. Filament current was adjusted during the process to control its thermionic electron emission and to maintain a constant substrate current density of ~0.13 mA/cm^2, so that resultant nitrogen diffusion and crystallographic evolution at material surfaces was mainly influenced by the different treatment temperatures (with the aid of radiant heating) and treatment times applied, rather than the different nitrogenous ionic bombardments. After treatment, samples were vacuum cooled (below 1×10^{-3} Pa chamber pressure) at a rate of approximately 3°C/min to 180°C, before venting to atmosphere.

2.3 Material Characterisation

Surface nitrogen content was evaluated using Energy Dispersive X-ray (EDX) spectroscopy via a Philips XL30S FEG scanning electron microscope equipped with Oxford Instruments INCA EDX system. Beam acceleration voltage, spot size and working distance were 15 kV, 5 and 5 mm, respectively. Beam intensity was calibrated

with a cobalt standard. The mean surface nitrogen content (and the 95% confidence interval) was derived from 10 random SEM-EDX measurements made over the nitrided surfaces, where each measurement location covered a sampling area of 65×45 μm.

A Nikon Eclipse LV150 Optical Microscope (OM) was used for optical imaging. The nitrided samples were cut transversely, mounted and polished to show cross-sectional features. The prepared sample cross-sections were etched using 50HCl-25HNO_3-25H_2O (in vol.%) and examined under OM, to reveal depth and morphology of the nitrogen diffusion zone. The mean layer depths (and 95% confidence interval) were evaluated from 50 cross-sectional measurements (i.e. 10 measurements each per micrograph, 5 micrographs in total). X-ray Diffraction (XRD) analysis was performed in conventional Bragg-Brentano geometry using a Bruker D2 PHASER instrument (Cu K-α radiation, 0.15418 nm). The tube voltage and current, step time, increment and scanning range were 30 kV and 10 mA, 0.4 s, 0.02° and 30° to 60°, respectively.

Thin foils for Transmission Electron Microscopy (TEM) were prepared perpendicular to the treated surface (i.e. in cross section) via Focused Ion Beam (FIB) milling, using a FEI Quanta 200 3D electron microscope, as shown in **Fig. 2**. A carbon layer was firstly deposited onto the site of interest, to protect the sample surface underneath from the damage of heavy-ion beam processing. Samples were milled and cut by the gallium ion beam (with an acceleration voltage of 30 kV) so that material underneath the carbon deposit could be lifted out perpendicular to the sample surface for cross-sectional viewing of thin sections. The extracted section was attached to a copper grid and then

thinned to <100 nm using successively smaller ion beam milling currents. The thinned areas were examined under TEM, using a Philips EM420 instrument at a beam acceleration voltage of 120 kV and a FEI Tecnai T20 instrument at 200 kV, to reveal morphological and crystallographic details. Bright-Field (BF) TEM images, Dark-Field (DF) TEM images and Electron Diffraction Patterns (EDP) were extracted from the ultra-thinned areas.

3 Results and discussion

3.1 Composition, morphology and XRD phase identification

Surface nitrogen atomic percentages (at.% N) and layer depths are evaluated and presented in **Table 2**. Treatment depths of both alloys after 4hrs of nitriding are at similar levels, but layer depths on AG17 are significantly larger than those on 330 after 20hrs of nitriding. The measured surface nitrogen contents (all > 20 at.% N) exceed significantly the equilibrium N-solubility (c.f. ~10.3 at.% in austenitic iron [54] and < 0.65 at.% for AISI 316 ASS [23]). Surface N contents of the nitrided alloy 330, which range narrowly between ~23 and 26 at.% N, are comparatively lower than those of the nitrided AG17 (between ~26 and 35 at.% N). Surface N content shows an expected increasing trend with treatment time, but such increase in surface N content with treatment time is much smaller on nitrided-330 compared to nitrided-AG17. Several optical micrographs of the TPN-treated surfaces are shown in **Fig. 3**. Individual grains can be clearly distinguished − due to different plasma etching effects on grains of varying crystallographic orientation − revealing an equiaxed polycrystalline

microstructure (with no 'macrozone'-like directionality) for the two alloys. The surface traces observed on nitrided alloy 330 (under top viewing in **Fig. 3c, d**) are confirmed on sample cross-sections (**Fig. 5b2, f2**) and will be discussed later with the TEM results.

XRD patterns of alloy AG17 and 330 indicate the formation of γ_N on both types of material after low-temperature TPN, according to the characteristic peak shifts to lower angles − which are also evident on the 450°C 4hrs nitrided 304 alloy (**Fig. 4**). The γ(200) peak always shifts more than the γ(111) peak for all three ASSs after TPN, in accordance with the first clearly documented XRD pattern of γ_N published by Ichii et al. in 1986 [9]. This occurs due to the fundamental elastic anisotropy of FCC structures (i.e. hkl-dependent lattice elastic constants) such that, under a specific elastic strain, the γ(200) peak will in any case shift to lower 2θ angles than does γ(111), since the non-close packed {200}γ planes are significantly more compliant than the close packed planes of {111}γ (e.g. $E_{111}/E_{001} = 3$ for AISI 316L, as estimated in [34]). The systematic study of lattice elastic anisotropy in cubic crystals can be traced back to the work of authors such as Zener et al. in 1948 [55]. An anisotropic "heavily strained austenitic structure" was the basis of the 'expanded austenite' terminology introduced by Leyland et al. in 1993 [11] to address the point that "asynchronous" peak shifts in XRD analysis are not in themselves indicative of the development of a new crystallographic phase – particularly when the existing phase possesses known elastic anisotropy.

As elucidated further by Sun et al. in 1999 [17], the apparently anomalous lattice

expansion in γ_N can in practice be attributed to a combined effect of residual stress and SF generation in the surface layer. Despite the different plasma conditions and ASS substrates used, the shifts of γ(111) and γ(200) XRD peaks for γ_N layers found in the literature appear very similar to those synthesised in this study (i.e. γ_N-304L [37] similar to the γ_N-AG17 generated at 400°C 20hrs; γ_N-316 [19] similar the γ_N-330 generated here). More importantly, comparisons between the peak shifts of AG17 and 330 under TPN indicate that γ_N-AG17 expands with both treatment time and temperature, while γ_N-330 exhibits rather invariant lattice expansion over the selected time/temperature ranges.

According to XRD profiles, γ_N-AG17 decomposed more readily than γ_N-304 with increasing treatment temperature and/or prolonged treatment time. The threshold decomposition condition for γ_N-304 lies somewhere between 4hrs and 20hrs at 450°C; however, γ_N-AG17 was clearly decomposed after only 4hrs at 450°C with α(110) and weak CrN(111) reflections seen under XRD measurements. Moreover, a weak 'hump' between 43.6° and 44.6° is seen for AG17 after TPN at 425°C for 20hrs, which corresponds to nanocrystalline ferrite formation, suggesting phase decomposition occurring also at 425° C (as confirmed later by TEM in **Section 3.3.1**). After TPN at 450°C 20hrs, the observable CrN(111) and α-Fe(110) peaks on both 304 and AG17 imply that the same phase decomposition mechanism is shared between γ_N-304 and γ_N-AG17. On the other hand, there is no direct evidence (from XRD) of CrN formation in γ_N-330 under the selected nitriding conditions of this study. However, a broad XRD 'hump' is observed near the substrate γ(111) peak position (i.e. ~43.8°), adjoined to the

γ_N(111) and γ_N(200) peaks at 450°C 20hrs − hinting at crystallographic arrangements other than γ_N (see further discussion in **Section 3.3.1**).

The transverse layer morphology is shown in **Fig. 5**. 'Deformation' traces are observed in both γ_N-330 and γ_N-AG17, owing to the heavily strained nature of the N-supersaturated layer. The high number density of deformation traces (sometimes 'woven' together) in γ_N-AG17 gives rise to rather dark regions just below the surface of AG17 treated at 400°C for 20hrs (as highlighted in **Fig. 5b1**). Similar traces are also evident in the γ_N-AG17 generated at the higher treatment temperatures (**Fig. 5c1, d1, f1**). On the other hand, surface layers on alloy 330 appear rather featureless, but deformation traces could also be seen parallel to each other in the treated layer; for example, after 20hrs at 400°C (as indicated with red arrows in **Fig. 5b2**). Compared to those seen in γ_N-AG17, the deformation traces in γ_N-330 are much fewer in number and are not interwoven with each other.

After 20hrs of TPN treatment at 425°C, dark regions (corresponding to decomposition products) are observed in the dominant bright phase of γ_N-AG17 (**Fig. 5d1**), giving solid evidence of phase decomposition (as also hinted at in the XRD profile of **Fig. 4b**). With a further increase in treatment temperature to 450°C, the surface layers on AG17 become double-layered (**Fig. 5e1** and **Fig. 5f1**), with a topmost decomposition layer and an underlying layer of γ_N-AG17. The observable γ_N-AG17 XRD peaks after 4hrs at 450°C (**Fig. 4b**) originated from the underlying layer. As the topmost layer (decomposed region) grew sufficiently thick with treatment time to exceed the X-ray

attenuation depth, only CrN and ferrite are detected after 20hrs of treatment (**Fig. 4b**). In contrast, the transverse surface layer microstructure on nitrided alloy 330 shows no indication of phase decomposition in γ_N-330, even at 450°C and 20hrs (**Fig. 5f2**). Nevertheless, cracks are probably initiated along 'deformation' traces and grain boundaries at 425°C 20hrs (as indicated with red arrows in **Fig. 5d2**) − and become significant at 450°C 20hrs (as indicated with red arrows in **Fig. 5f2**).

3.2 Discussion of TEM observations on γ_N

3.2.1 General observations on TEM lattice parameters of γ_N

TEM lattice parameters (a_{111} and a_{200}) of γ_N can be calculated from the distances of the respective diffraction spots to the centre spot in EDPs. Firstly, as the high compressive stress of γ_N diminishes during preparation of thin TEM foils (i.e. stress relaxation occurs when the anisotropically strained γ_N is no longer constrained by the bulk material volume), the measured EDP lattice parameters appear almost hkl-independent (i.e. $a_{111} \approx a_{200}$), apparently revealing an almost isotropically expanded austenite − as also noticed in TEM studies of γ_N-316 [19]. Secondly, assuming an invariant camera constant (i.e. $\lambda \times L$) for all EDPs, using a TEM sample of untreated RA 330® for calibration (taking $a_{111} \approx a_{200} \approx$ ~0.358 nm), TEM lattice constants of γ_N thin foils extracted from 400°C 20hrs treated surfaces are ~0.390 nm for γ_N-AG17 and ~0.381 nm for γ_N-330, clearly indicating the persistence of lattice expansion under stress-free (or "micro-stress") conditions. Noticeably, the measured TEM lattice parameter of γ_N decreases from surface to core and the abovementioned lattice parameter values of γ_N-

AG17 and γ_N-330 were measured next to the surface of cross-sectional TEM thin foils (using a ~500 nm diameter diffraction aperture). However, such 'quantitative' analysis is non-representative and probably inaccurate, owing to small sampling areas, small errors in camera length (despite placing the sample at the eucentric height), influences from the FIB preparation process, etc; hence the lattice parameters derived from TEM measurement are not discussed further.

3.2.2 TEM observations

As revealed in **Section 3.1**, AG17 and 330, having significantly different substrate chemical composition (and thus SFE), show very different lattice-expansion behaviour with treatment time and temperature under XRD. After TEM observation, we found that i) the increasing XRD peak shift (to lower angles) of γ_N-AG17 with temperature/time correlates well to the evolution of lattice distortion observed under TEM, and ii) the relatively invariant lattice expansion of γ_N-330 correlates to a rather 'perfect' FCC lattice (with low SF density).

After 4hrs of nitriding at 400°C, γ_N-AG17 shows only austenitic diffraction intensity maxima under TEM (**Fig. 6a**), whilst a high SF density is obtained in γ_N-AG17 after 20hrs of treatment at the same temperature (**Fig. 6b**). The $<111>\gamma_N$ 'streaking' (**Fig. 6b**) corresponds to a high SF density on $\{111\}\gamma_N$ planes, which correlates to the further composition-induced lattice expansion with time. Although it was not unambiguously observed or reported in the open literature of expanded austenite, this $<111>\gamma_N$

streaking (under N-induced strain) could occur as a result of dissociation of 'perfect' dislocations into Shockley partials on the $\{111\}\gamma_N$ slip planes (e.g. $\frac{a}{2}[110] \rightarrow \frac{a}{6}[211] + \frac{a}{6}[12\bar{1}]$, where a denotes the lattice parameter), which is normally considered responsible for the <111>γ streaking observed in mechanically deformed FCC alloys. Through dislocation dissociation, lattice strain is accommodated by the generation of SFs on $\{111\}\gamma_N$ planes. A secondary set of intensity maxima is observed on the $<111>\gamma_N$ streaks, corresponding to the same bright strip-shaped regions at the nitrided surface, which are revealed by DF-TEM imaging of the intensity maxima (**Fig. 6c-e**). These maxima are indexed as HCP ε-martensite. After 20hrs of nitriding at 400°C, these parallel bright HCP strips are ~10-40 nm wide and occupy approximately ~24% volume fraction at the material surface investigated under TEM. Similar to the 'clustered SFs' reported by Tong et al. [37] in γ_N-304L or 'primary ε bands' by Lee et al. [40] in plastically deformed low SFE ASS, the ε-martensite and parent γ_N-AG17 follow the Shoji-Nishiyama (S-N) structure-orientation relationship, i.e. $<110>_{\gamma N}//<2\bar{1}\bar{1}0>_{\varepsilon}$ and $\{111\}_{\gamma N}//\{0001\}_{\varepsilon}$. These strips can be considered as a local distortion of the FCC austenitic structure (with a high SF probability of ~0.5), in which case SFs are present on every second $\{111\}\gamma_N$ plane. Noticeably, no evidence of twinning was observed in EDPs under TEM. A third set of weak intensity maxima can also be observed − and these were examined more closely under DF-TEM (**Fig. 6f**). No clearly distinguished responsible features could be found, indicating that these weak diffraction reflections are unlikely to originate from the ε-martensite strips. Such weak reflections are however evident not just in γ_N-AG17, but also in γ_N-304 [37], γ_N-316 [18,

19, 38] and γ_N-316L [39]. In the model of Jiang et al. [18], these weak diffraction patterns are claimed to correspond to 'forbidden' reflections of γ_N − and are attributed to ordered occupation by N at the centre of corner-sharing octahedra in the FCC lattice.

At a treatment temperature of 425°C, similar structural evolution with time is revealed in γ_N-AG17. The EDP of γ_N-AG17 treated at 425°C for 4hrs (**Fig. 7b**) presents γ_N spots and $<111>\gamma_N$ streaking. The EDP of γ_N-AG17 treated at 425°C for 20hrs (**Fig. 7f**) presents γ_N spots, $<111>\gamma_N$ streaking – and also HCP spots and 'forbidden' γ_N spots. In the DF-TEM image of the 425°C 20hrs nitrided AG17 surface using a single HCP spot (**Fig. 7d**), parallel strips are revealed inside the regions of γ_N-AG17 that has not decomposed to CrN + α.

Additionally, comparisons between the 400°C treated γ_N-AG17 samples and the 425°C ones reveal a structural evolution with treatment temperature. The extra $<111>\gamma_N$ streaking in the EDP of γ_N-AG17 at 425°C 4hrs (**Fig. 7b**), as compared to γ_N-AG17 at 400°C 4hrs (**Fig. 6a**), corresponds to a slightly larger lattice strain. The EDP features of the γ_N-AG17 at 425°C 20hrs (**Fig. 7f**) are the same as those at 400°C 20hrs (**Fig. 6b**); however, comparing the DF-TEM images of γ_N-AG17 at 425°C 20hrs (**Fig. 7d**) and at 400°C 20hrs (**Fig. 6d**), the HCP lamellae evidently grow in width (from ≤ 30 nm to ≤ 50 nm) and in volume fraction (from ~24 vol% to ~37 vol%) with the increase in treatment temperature from 400°C to 425°C.

In contrast, mainly FCC diffraction spots are observed in EDPs of γ_N-330 synthesised at 400°C 20hrs (**Fig. 8a)** and at 450°C 20hrs **(Fig. 9b)**. The γ_N-330 synthesised at 425°C 20hrs was not examined under TEM, but should have a similar crystallographic structure to the γ_N-330 synthesised at 400°C 20hrs, owing to the similar measured surface nitrogen content and XRD profile. Noticeably, the $(200)\gamma_N$ and $(220)\gamma_N$ reflections in **Fig. 9b** appeared 'stretched' towards the centre spot, hinting at crystallographic structures other than γ_N (see **Section 3.3.1**).

No evidence of SFs, twins or HCP martensite is observed in γ_N-330 − suggesting a nearly 'perfect' FCC lattice (with low SF density) of alloy 330 after nitrogen-interstitially introduced lattice expansion. In this case, the rapid saturation of the lattice expansion observed for γ_N-330 could be correlated primarily to dislocation slip (e.g. $\{111\}\gamma_N<110>\gamma_N$ as active primary slip systems) under the thermochemically-induced lattice strain. Intriguingly, the forbidden γ_N reflections are absent in γ_N-330, despite the interstitial nitrogen content apparently exceeding the level required to saturate the FCC lattice octahedral centres. In contrast to ordered occupation suggested for γ_N-316 by Jiang et al. [18], the nitrogen occupation might be 'random' in γ_N-330, potentially owing to a rather low interstitial N occupation in octahedral 'trap sites' in the vicinity of the (randomly distributed) Cr atoms in the FCC lattice.

Additionally, microscopic shear bands (i.e. localised accumulation and interaction of shear planes) are evident inside γ_N-330 grains under TEM (**Fig. 8b, c**). Similar shear bands, which initiate through structural instability (and contain layered dislocation

walls), have been reported on plastically deformed (i.e. cold-rolled) high- or medium-SFE materials [56, 57]. The shear band investigated here can be classified as a 'copper-type' shear band (rather than 'brass-type') − according to the terminology introduced by Wagner et al. [58] − since there is no evidence of twin lamellae. In the EDP of **Fig. 8b**, apart from γ_N diffraction spots (arising from an adjacent γ_N-330 grain), the obvious 'spot-and-stripe' intensity pairs and weak 'amorphous' diffraction rings suggest lattice misorientation and distortion within shear bands under highly localised strain.

Under DF-TEM imaging using one of the intensity maxima (**Fig. 8c**), the shear band discussed above appears to be ~120 nm wide. Extensive dislocation interactions within this shear band have caused the volume to the left of the shear band (**Fig. 8c)** to be displaced out from the material surface − presumably under compression parallel to material surface. This observation of high-level plasticity confirmed the deformation traces observed under OM (**Fig. 3c** and **Fig. 5b2**). Unlike the large volume fraction of HCP lamellae observed at the surface of γ_N-AG17 − where such outward volume displacements under compression were small or gradual and the associated deformation traces were not too clear under top-viewing using light OM (**Fig. 3a**) − the shear bands in γ_N-330 are 'macroscopically' located several microns from each other in the austenite grains and the associated deformation traces were very obvious in **Fig. 3c**. Given such localised dislocation-mediated microstructural evolution and volume displacement along shear bands, one could assume dislocation accumulation and interactions at grain boundaries. In addition to the expansion/strains developed, such dislocation

accumulations could initiate voids and eventually micro-cracking along shear bands and grain boundaries, as observed in γ_N-330 (**Fig. 5d2, f2**).

3.2.3 Effect of SFE on composition-induced deformation mechanisms of γ_N

Various local features of lattice distortion, including SFs, twinning and/or local 'martensitic' SF clusters, have been reported and studied in expanded austenite layers synthesised on AISI 304L [37], AISI 316 [18, 19, 38] and AISI 316L [39] after plasma nitriding. The HCP-structured 'strips' observed by Tong et al [37] in γ_N-304L (similar to those observed in γ_N-AG17) were considered as clustered SFs − which was attributed to the small widths of the HCP features observed (no more than about ten nanometers wide). However, the 'primary ε bands' identified in the study by Lee et al. [40] are clearly also less than ten nanometers wide. The HCP strips observed in γ_N could actually be considered as ε-martensite, equivalent to regions (in bands or strips) with high SF densities on $\{111\}\gamma_N$ planes having ABABAB arrangement (ε-martensite) rather than ABCABC arrangement (γ-austenite).

Most importantly, the abovementioned local lattice distortion of γ_N bears close analogy to the structure of plastically deformed Mn/N-stabilised ASS reported by Lee et al. in [40], which has been illustrated in **Fig. 1.** For the observable $\{111\}\gamma_N$ SFs (and the potential for lattice twinning and/or martensitic transformation), the composition-induced lattice strain has a similar effect on the austenitic lattice compared to mechanical strain; in which case, the (composition-related) SFE is an essential material

property in low temperature diffusion treatment of ASS. Lee et al. [40] experimentally identified and discussed three SFE regions for mechanically deformed high interstitial ASSs, which were i) SFE < 15 mJ/m^2 for only martensitic transformation; ii) 15 mJ/m^2 < SFE < 20 mJ/m^2 for the co-existence of deformation twins and martensite; iii) SFE > 20 mJ/m^2 for the occurrence of deformation twins only. Additionally, modeling of SFE using the Gibbs free energy of the austenite to martensite transformation, $\Delta G^{\gamma \rightarrow \varepsilon}$, suggests a threshold SFE at ~18 mJ/m^2 [49, 59]. In other words, the strain-induced HCP ε-martensite transformation is energetically favourable for materials with SFE below ~18-20 mJ/m^2.

From our studies (and from the available literature), the ε-martensite in γ_N-AG17, the coexistence of ε-martensite and twins in γ_N-304L [37], the lattice twinning in γ_N-316 [38] (or nano-twins in γ_N-316L [39]), and the low SF density in γ_N-330, all correlate well to their respective substrate SFEs (i.e. following an order from low SFE to high, AG17 → 304 → 316 → 330), implying a likely correlation between substrate SFE and specific, localised lattice distortion under nitrogen-interstitial induced strain. Similar to the effects of mechanical strain, one might further postulate local displacive transformations of γ_N to i) martensite only with SFE < 15 mJ/m^2; ii) a mixture of martensite and twins with SFE from 15 to ~18-20 mJ/m^2; iii) twins only with SFE > 20 mJ/m^2. One could qualitatively rank the SFE of γ_N (at a typical nitriding temperatures of ~400°C) from low to high as γ_N-AG17, γ_N-304(L), γ_N-316(L) and γ_N-330 − which follows the SFE trend of substrate compositions from Mn-stabilised ASS to Ni-stabilised ASS.

3.2.4 The 'real' SFE of γ_N during nitriding

The deformation modes discussed so far have been correlated to the SFEs of unmodified substrates, which are hinted at by the literature and – as confirmed in this study for γ_N-AG17 and γ_N-330 – present distinguishably different 'deformation structures'. However, the distortion mechanisms are in practice determined by the 'dynamic' (nitrogen-concentration mediated) SFEs of the near-surface FCC lattices generated during treatment − rather than the 'textbook' room-temperature (unmodified) substrate SFE values – with consideration of the effects from both treatment temperature and local chemical composition on SFE.

The interactions between nitrogen and different host systems (e.g. Fe-Cr-Ni-N and Fe-Cr-Mn-N) will result in incomparable N-dependence of SFE amongst different systems. Experimentally, SFE was reported as decreasing linearly with increasing N-content in the Fe-Cr-Ni-N system [41], while the effect of N on SFE appeared non-monotonic in the Fe-Cr-Mn-N system [40, 48, 49]. Increasing N-content in the Fe-Cr-Mn-N solid solution initially decreases SFE, due to Suzuki segregation of N into (and locking) SFs at low N-concentration and then increases SFE at higher N-contents, due to the less effective interstitial segregation [49]. However, available literature on SFEs of N-containing ASSs (e.g. [40, 41, 48, 49]) was based on measurements/models for N-contents in the low concentration regime − i.e. below 0.8 wt.% (~3 at.%) − at room temperature. The real effect of N on SFE − especially in the "colossal supersaturation"

[60, 61] concentration region at nitriding temperatures − is complex and requires further systematic investigation beyond the immediate scope of this paper.

SFE should increase with temperature for ASSs (and presumably for the γ_N synthesised on ASSs), whereby the energy required on generating SFs will rise commensurately with nitriding treatment temperature. The 'locking' effect of interstitial N on SFs is likely to be reduced by the thermally-enhanced mobility of interstitial N at typical thermochemical diffusion treatment temperatures, increasing SFE, but the much higher N-content (and short-range ordering of Cr-N) could contribute to SFE in an opposite way, creating energy barriers for dislocation glide, thus decreasing SFE. For example, the distorted structures observed in γ_N-AG17 (i.e. only ε-martensite for SFE probably less than 15 mJ/m^2) can be attributed to the extensive short-range-ordering of Cr-N clusters, which creates energy barriers in the slip systems (decreasing SFE), offsetting the influence of raised temperature. The low SF density (or SF-free) features of γ_N-330 could certainly be attributed to its high SFE – and to the increase in SFE with temperature. However, the high N content could also offset the influence of raised temperature in γ_N-330. The initiation of strain localisation (i.e. shear banding) in γ_N-330 might be due to local interference of Cr-N clusters with dislocation glide.

Moreover, the discussions on SFE of γ_N above are based on some 'precise' SFE values/ranges for the four types of ASS substrates being considered. For the two special ASS substrates investigated in this study, only the major alloying elements (viz. Ni, Mn and N) were considered in estimating substrate SFEs. However, there are small but not

insignificant amounts of other alloying elements in the two special ASSs (i.e. Si, Co, Al, Ti, Cu and C in **Table 1**), which could also influence material SFE/deformation mode. There is an inherent lack of data on the SFE of the two substrate alloys used in the present work. Nevertheless, given the extremely high interstitial N content in γ_N (cf. the low interstitial levels of N/C in the ASS substrates), the SFE of γ_N during nitriding should mainly be influenced by the various substitutional alloying elements (and to a much lesser extent the interstitial elements) already present in the substrate. Strong nitride formers in ASSs (such as Al and Ti in alloy 330) might reduce the SFE of γ_N via short-range ordering with N (similar to that of Cr-N clusters). However, with the low SF densities found in γ_N-330 from our various TPN treatments performed here, the positive influence on SFE from high Ni content and elevated temperature appears to prevail.

3.2.5 Implication of SFE-dependent plasticity on the structure of γ_N

If we are allowed to consider the plastic accommodation of the extremely high interstitial nitrogen absorption in γ_N as a uniaxial tension outward from the surface plane, the out-of-plane tensile-like deformation (and the resultant crystallographic structure) of a typical γ_N layer on ASS − that originates from lattice volume expansion owing to N-insertion (and the surrounding material volumes restricting such expansion) – would be influenced by i) nitrogen concentration profile, ii) non-linear hkl-dependent nitrogen-introduced lattice strain [24, 36] and iii) orientation-dependent nitrogen-introduced lattice rotation [33, 35].

Firstly, interstitial N-uptake should depend on the substrate composition and nitriding condition, in which case − from a chemical point of view − the different Mn/Ni contents in two ASS substrates (at a similar Cr level) influence the paraequilibrium N-solubility in γ_N under equivalent treatment conditions. Nevertheless, apart from the chemical aspect, lattice defects (such as SFs and partial/perfect dislocations) generated upon interstitial accommodation of nitrogen might further enhance the paraequilibrium nitrogen solubility in both γ_N-AG17 and γ_N-330. Typically, a positive correlation between SF density and N-uptake was seen for γ_N-AG17 during treatment, while γ_N-330 − under the retention of a 'perfect' FCC lattice with little or no SFs – exhibited rapid nitrogen saturation at rather low nitrogen concentrations (and an associated limit of lattice expansion). The high surface N-uptake (and lattice expansion) of γ_N-AG17 should be largely due to the high-Mn content (with negligible Ni) – which is normally known as enhancing the equilibrium solubility of interstitial nitrogen in ASS; however, the extra defects generated under such high N-absorption in a high-Mn content austenite lattice might also contribute to the enhanced interstitial nitrogen accommodation. It should nevertheless be highlighted that there is currently no direct evidence of defect-enhanced N-absorption in γ_N and further experimentation (on defect number density and/or local chemistry) would ideally be required to validate our suppositions.

The plastic deformation of γ_N is accommodated by the generation of dislocations and displacive lattice rearrangements (via dislocation-mediated plasticity mechanisms) on activated slip systems. Most importantly, the SFE-dependent plasticity mechanisms (e.g. deformation slip, twining, martensitic transformation, or combinations thereof) will

strongly influence material strain hardening behaviour. The different strain hardening effect (with respect to SFE and plasticity mechanism) − in combination with solid solution strengthening effect − would give rise to different hkl-dependent lattice-expansion (or 'mechanical' behaviour) of the N-supersaturated lattice under composition-introduced strain (or out-of-plane tensile-like deformation) during treatment. However, the Taylor-Bishop-Hill model [62-64] and the self-consistent model by Clausen et al. [65] discussed in the literature (Ref. [35] and [24], respectively) for the composition-introduced plasticity in γ_N-316L assume deformation slip only, where the potential dislocation dissociation, associated deformation mechanisms (other than slip), and formation of local misorientation in γ_N-316L (or in γ_N with lower SFEs) were not considered. For example, the potential twinning mechanism (e.g. formation of nano-twins as reported in [39]) in conjunction with dislocation slip might contribute to the discrepancies between predicted (based on slip-only models) and experimental results in lattice rotation of the γ_N-316L layer [35] and in XRD lattice parameters of γ_N-316L powder [24], especially for both forms of γ_N-316L argued as experiencing plastic deformation in the respective literature. On the other hand, the high SFE γ_N-330 (believed predominantly to exhibit dislocation glide under composition-introduced strain) might fit better to those plasticity models that consider only slip, but the shear banding observed in γ_N-330 from the present work indicates another aspect for consideration.

Apparently, the structure models for γ_N (if developed further in the future) would vary with the plasticity mechanisms that could occur, which are in turn sensitive to the SFEs

of the N-supersaturated material volumes generated. This points to a need for future investigations to unravel the complex parameter-interactions leading to the structure of γ_N, which might typically involve numerical simulation/modeling in plastic deformation of polycrystalline FCC lattices (with different SFEs) and/or low-temperature nitriding of a range of bespoke Cr-containing austenitic 'model' alloys (designated for specific SFEs). The discrepancies between material deformation behaviour under tensile strain at elevated temperatures and under N-introduced strain at equivalent nitriding temperatures might help to clarify the role of Cr-N clustering in γ_N on lattice plasticity. To facilitate this, it would be relatively easier to start with a polycrystalline FCC alloy of high SFE (such as alloy 330), where deformation glide is promoted over other plasticity mechanisms.

3.3 Discussion of TEM observations on γ_N decomposition

3.3.1 TEM observations

In comparison with XRD, TEM analysis indicates slightly different (and arguably more precise) results. The threshold decomposition condition for γ_N-AG17 is determined, almost exactly, as 4hrs at a treatment temperature of 425°C (**Fig. 7a-c**). The selected area EDP of **Fig. 7c** reveals CrN and α-ferrite diffraction rings (identified by PDF cards 01-076-2494 and 00-006-0696, respectively) in the topmost region of the diffusion layer only, which presumably has the highest nitrogen content and lattice distortion. The precipitation morphology of CrN in plasma nitrided AG17 is comparable to that of plasma nitrided 304 in **Fig. 10**, where fine lamellar CrN precipitates (with an inter-

lamellar spacing of only 1-3 nm) were observed for both 304 and AG17 after TPN at 450°C and 20hrs (**Fig. 10c**). Similar thin, lamellar CrN precipitation (with inter-lamellar spacing of 3-5 nm) has also been reported by Li et al. [38] in decomposed γ_N-316 − which was attributed to a cellular precipitation mechanism under low diffusivity of Cr. Noticeably, γ(111) halos are observed in between the CrN(111) ring and the α-Fe(110) ring in the EDPs of **Fig. 10b** and **Fig. 10e**, suggesting residual austenitic structure in the decomposed lattice for both AG17 and 304. Therefore, γ_N-AG17 and γ_N-304 experienced a eutectoid phase transformation, which is: $\gamma_N \rightarrow CrN + \alpha\ (+ \gamma)$. However, considering the phase decomposition mechanism of γ_N-304L to CrN + α-ferrite [52], the observed residual γ(111) halos are most likely due to incomplete phase transformation caused by sluggish substitutional element diffusion kinetics at the treatment temperature. It is also worth mentioning that Mn_3N_2 precipitation, which was reported for the high-Mn alloy Fe-18Cr-11Mn-3Mo [50] after plasma nitriding, is not observed in γ_N-AG17.

For alloy 330, grain boundary precipitates are clearly seen after 450°C 20hrs treatment (**Fig. 9c, d**). In the EDP of **Fig. 9c**, the large diffraction spots originate from two adjacent grains of γ_N-330 within the diffraction aperture, whilst the polycrystalline diffraction rings can be indexed as CrN and (Ni stabilised) γ-Fe co-located at (or near) the grain boundary − identified by PDF cards 01-076-2494 and 00-052-0513, respectively. **Fig. 9d** reveals nanometric clusters of spheroidal precipitates, the precipitation zone being ~150 nm wide. More importantly, further to the 'stretched' diffraction spots (**Fig. 9b**) observed for γ_N-330 at 450°C for 20hrs, fine spheroidal nano-sized 'particles' are seen in BF-TEM imaging (**Fig. 11a, c**) and the 112 zone axis EDPs

(**Fig. 11 b, d**) suggested secondary phase(s) in γ_N-330. Phase decomposition occurs (sluggishly) inside γ_N-330 grains after TPN at 450°C for 20hrs. Taking the lattice parameters of CrN, γ-Fe and γ_N-330 as, respectively, ~0.414 nm (PDF card 01-076-2494), ~0.366 nm (PDF card 00-052-0513) and ~0.380 nm (estimated from 111 plane XRD peak position of γ_N-330 layer at 450°C and 20hrs), the lattice parameter ratios can be determined as i) ~1.09 between CrN and γ_N-330, and ii) ~1.13 between CrN and γ-Fe. The diffraction distance ratio of the measurable adjacent spots (from **Fig. 11b, d)** is ~1.10, which is very close to the value expected between CrN and γ_N-330, hinting that CrN is nucleated coherently within the γ_N-330 grains.

Additionally, and in contrast to the sharp polycrystalline spots observed at grain boundaries, the different sets of diffraction spots for the FCC phases inside γ_N-330 grains (**Fig. 11b, d**) are very close together. The broad XRD 'hump' near the γ(111) position at 450°C 20hrs (**Fig. 4c**) could be attributed to the formation of (Ni-stabilised) unexpanded γ-Fe inside γ_N-330 grains (in accompaniment to CrN formation), where diffraction maxima of γ-Fe and γ_N-330 might overlap in EDPs (**Fig. 11b, d**), owing to the close lattice parameters and potential coherency between them. Line broadening in the XRD profile of this sample could be due to the small size of phases nucleated, potential coherency-microstrain (between γ-Fe and matrix for their close lattice parameters and structures), and the nitrogen-concentration or microstrain gradient (from surface to core) in the γ_N-330 layer. The bright 'particles' observed in **Fig. 11a, c** could be early-stage decomposed regions that contain mixtures of CrN, γ-Fe and/or γ_N-330. Inside the γ_N-330 grains, the nucleated phases and the untransformed matrix follow a

'cube-on-cube' orientation relationship, i.e. $<110>_{\gamma}//<110>_{CrN}//<110>_{matrix}$ and $\{111\}_{\gamma}//\{111\}_{CrN}//\{111\}_{matrix}$. This decomposed structure inside γ_N-330 grains should be metastable, i.e. a progressive loss of phase coherency is expected with increasing treatment temperature (or prolonged treatment time).

The abovementioned sluggish decomposition of γ_N-330 (inside grains and at grain boundaries) is observed for the entire TEM foil shown in **Fig. 9a**, which covers an area from the material surface to a depth of ~5.5 μm. The decomposition mechanism can be determined for γ_N-330 as being: $\gamma_N \rightarrow$ CrN + (Ni-stabilised) γ-Fe, which is similar to that frequently reported for γ_N-316, e.g. Ref. [38]. Noticeably, given the high Cr content in the γ_N-330, the nitride phase is indexed as CrN. However, considering the strong chemical affinity of Al/Ti (as minor additions in alloy 330) for N, Al and Ti might also be present in the CrN-type phase(s) both inside γ_N-330 grains and at grain boundary regions. The nitride phase(s) could thus be of the form (Cr, Al, Ti)N − or possibly a mixture of CrN/(Cr, Al)N and TiN/(Ti, Al)N.

3.3.2 Influence of SFE on the phase decomposition of nitrogen-expanded austenite

The strong chemical affinity of Cr for N eventually leads to CrN formation in both AG17 and 330 during low-temperature nitrogen diffusion treatment. Notwithstanding the HCP martensitic transformation in γ_N-AG17 (and local lattice misorientation in γ_N-330), in this paper we define 'phase decomposition' with respect to the formation of chromium nitrides, which requires segregation and redistribution of substitutional

elements to nucleate and grow new precipitates of a fundamentally different chemical composition and crystallographic structure – in particular because of its significance to material corrosion properties in practical applications. The formation of nitrides in γ_N is limited during low-temperature nitriding treatment − and is controlled mainly by the diffusivity of substitutional elements, which clearly will vary with material composition.

Moreover, given the limited substitutional diffusivity at the low treatment temperatures involved, lattice instabilities (e.g. SFs and ε-martensite) would play a vital role in promoting the formation of distinct nitride crystallographic phases during treatment. Phase decomposition of γ_N-AG17 at 425°C initiates from the topmost region of the nitrided surface, where lattice expansion and SF density should be the highest. The precipitation of CrN in γ_N-AG17 is facilitated by substantial lattice strain, high SF density and the formation of ε-martensite. Phase decomposition of γ_N-AG17 occurred allotropically to α-Fe + CrN in a similar way to that commonly reported for γ_N-304, but the threshold decomposition condition was lowered (from 450°C 4hrs for γ_N-304 to 425°C 4hrs for γ_N-AG17 in this study), which can be correlated to the lower SFE expected of AG17 ($10 \leq 18$ mJ/m^2 for unmodified AG17 compared to ~18 mJ/m^2 for unmodified 304).

On the other hand, compared to the 'complete' phase decomposition in γ_N-AG17 and γ_N-304 at the upper treatment conditions of 450°C and 20hrs, γ_N-330 was still at the early stages of decomposition under these conditions, where XRD and TEM results hinted at formation of decomposition products in the γ_N-330 layer but an apparently

mono-phased 'white' layer was still observed after etching (**Fig. 5f2**). Owing to the free surface provided (i.e. high interfacial energy planar defects) and the relatively high substitutional diffusivity in the grain boundary regions, phase decomposition of γ_N-330 occurred more readily at grain boundaries, where nano-sized polycrystalline CrN and γ-Fe precipitates were observed. Such sluggish decomposition of γ_N-330 could be attributed to the minor lattice instabilities in γ_N-330 grains and correlates well to the significantly higher SFE of unmodified alloy 330. High SFE materials appear thermodynamically more stable, as compared to low SFE ones (e.g. 304 and AG17) upon low-temperature nitrogen-supersaturation. Apart from the SFE aspect, the additions of Al and Ti in alloy 330 (although very small in content) might also enhance the stability of γ_N-330. Christiansen et al. [66] recently illustrated an alloy design principle based on a concept that strong nitride/carbide forming elements (such as Al and Ti) could hinder the formation of chromium nitrides/carbides and thereby potentially raise the thermodynamic stability of expanded austenite, after observing γ_N layers (with no signs of CrN formation) on an austenitic precipitation hardening stainless steel (viz. A286, containing ~2 wt.% Ti, 0.35 wt.% Al) under gaseous nitriding at 500°C for 14hrs.

Conclusions

In summary, this study characterised and compared the structure of two austenitic lattices; a N-containing high-Mn one (with low SFE) and a high-Ni one (with high SFE), both with similar Cr contents of ~17-19 wt.%) after low-temperature TPN treatment –

with the widely-studied AISI 304 alloy also employed, as a benchmark. The analogy between composition-induced strain and mechanical strain in ASS was illustrated and further confirmed by TEM observations.

1. Two possible types of composition-induced plasticity mechanism were revealed in γ_N with respect to material SFE, after the TEM observation of i) HCP lamellae (or ε-martensite) in a high SF density γ_N-AG17, via dislocation dissociation, and ii) a relatively low SF density (or SF-free) γ_N-330, via dislocation glide, with small volumes of shear bands. At higher treatment temperatures, two possible 'diffusional' phase decomposition mechanisms were identified, which are: i) a uniformly distributed eutectoid decomposition mechanism to CrN + α-Fe in AG17, and ii) sluggish CrN formation inside grains (but polycrystalline precipitation at grain boundaries) to CrN + (Ni-stabilised) γ-Fe in alloy 330.
2. Other than providing the basic (meta)stable room-temperature austenitic phase composition of the parent alloy, neither Mn nor Ni is essential for formation of γ_N, but each element has a pronounced effect on the expanded lattice structure and stability resulting from low-temperature thermochemical treatment, via their influence on SFE – and particularly with regard to the onset of crystallographic phase instability at the point of alloy 'over-supersaturation' with nitrogen (in Fe-Cr-Ni/Mn-N systems) for specific, alloy composition-dependent, critical temperature/time envelopes. A symbiotic relationship between SF number density and nitrogen uptake was seen in the γ_N-AG17 of the low-SFE alloy during thermochemical treatment, but also tended to result in accelerated phase

decomposition at higher treatment temperatures. Given the potential slip under lattice strain, nitrogen-supersaturated high-SFE alloys (such as γ_N-330) tend to accommodate less interstitial nitrogen overall − with rapid saturation (and relatively low anisotropic expansion) occurring under thermochemical treatment) − but exhibit better structural integrity and thermodynamic stability.

As a final point, whereas (historically) significant effort has been expended in designing "nitridable" ferritic alloys for commercial applications, little or no commercial effort has been made to develop analogous austenitic grades amendable to low-temperature plasma diffusion treatment − due in no small part to the sheer complexity of the chemical composition-dependent issues which the metallurgical behaviour of an elastically anisotropic parent lattice (with strongly composition-dependent strain behaviour and lattice instability) introduces. In this regard, the work reported here takes several tentative steps towards improved material selection criteria − and a basic design methodology − for developing improved 'nitridable' austenitic engineering alloys for specific applications. Apart from Mn and Ni, various other substitutional elements (e.g. Al, Ti, Si, Mo, Co, Cu etc.) can also influence the SFE and/or lattice stability of ASSs (and other austenite-containing alloys), pointing to the need for future studies on low SFE austenitic alloys (e.g. Cr-containing TWIP/TRIP steels or Co-Cr alloys) and/or high SFE alloys (e.g. superaustenitic ASSs or Ni-Cr alloys) under low-temperature thermochemical diffusion treatment. The potential lattice twinning and/or martensitic transformation in Cr-containing TWIP/TRIP steels under low-temperature nitrogen supersaturation could substantially influence material structure-property-performance

considerations, particularly for optimal design of future thin-section, high-strength, light-weight steel structures.

Acknowledgements

This research did not receive any specific grant from funding agencies in the public, commercial, or not-for-profit sectors. We would however like to thank ATI Allvac (Sheffield) Ltd. for their kind provision of Staballoy AG17® and NeoNickel (Blackburn) Ltd. for supply of RA 330® for this study.

References

[1] O.C. Shepard, The effect of carbide precipitation and carburisation on the mechanical properties of type 304 stainless steel, U.S. AEC Report 1958.
[2] W.C. Hayes, O.C. Shepard, Corrosion and decarburization of the ferritic chromium-molybdenum steels in sodium coolant systems, Atomics International, 1958.
[3] W.J. Anderson, G.V. Sneesby, Carburization of austenitic stainless steel in liquid sodium, Atomics International, 1960.
[4] W.F. Holcomb, Carburization of type 304 stainless steel in liquid sodium, Nucl. Eng. Des. 6 (1967) 264-272.
[5] F.B. Litton, A.E. Morris, Carburization of type 316L stainless steel in static sodium, J. Less-Common Met. 22 (1970) 71-82.
[6] B.H. Kolster, Mechanism of Fe and Cr transport by liquid sodium in non-isothermal loop systems, J. Nucl. Mater. 55 (1975) 155-168.
[7] M.A.J. Somers, T. Christiansen, Low temperature surface hardening of stainless steel in: E.J. Mittemeijer, M.A.J. Somers (Eds.), Thermochemical Surface Engineering of Steels, Woodhead Publishing, Cambridge, 2015, pp. 557-579.
[8] Z.L. Zhang, T. Bell, Structure and corrosion resistance of plasma nitrided stainless steel, Surf. Eng. 1(2) (1985) 131-136.
[9] K. Ichii, K. Fujimura, T. Takase, Structure of the ion-nitrided layer of 18-8 stainless steel, Technol. Rep. Kansai Uni. 27 (1986) 135-144.
[10] D.L. Williamson, L. Wang, R. Wei, P.J. Wilbur, Solid solution strengthening of stainless steel surface layers by rapid, high dose, elevated temperature nitrogen ion implantation, Mater. Lett. 9 (1990) 302-308.
[11] A. Leyland, D.B. Lewis, P.R. Stevenson, A. Matthews, Low temperature plasma diffusion treatment of stainless steels for improved wear resistance, Surf. Coat. Technol. 62 (1993) 608-617.
[12] D.L. Williamson, O. Ozturk, Metastable phase formation and enhanced diffusion in f.c.c. alloys under high dose, high flux nitrogen implantation at high and low ion energies, Surf. Coat. Technol. 65 (1994) 15-23.
[13] Y. Sun, T. Bell, Sliding wear characteristics of low temperature plasma nitrided 316 austenitic stainless steel, Wear 218 (1998) 31-42.
[14] D.L. Williamson, J.A. Davis, P.J. Wilbur, Effect of austenitic stainless steel composition on low-energy, high-flux nitrogen ion beam processing, Surf. Coat. Technol. 103-104 (1998) 178-184.
[15] K. Marchev, M. Landis, R. Vallerio, C.V. Cooper, B.C. Giessen, The m phase layer on ion nitrided austenitic stainless steel (III), an epitaxial relationship between the m phase and the γ parent phase and a review of structural identifications of this phase Surf. Coat. Technol. 116-119 (1999) 184-188.
[16] E. Menthe, K.T. Rie, Further investigation of the structure and properties of austenitic stainless steel after plasma nitriding, Surf. Coat. Technol. 116-119 (1999) 199-204.
[17] Y. Sun, X.Y. Li, T. Bell, X-ray diffraction characterisation of low temperature plasma nitrided austenitic stainless steels, J. Mater. Sci. 34 (1999) 4793-4802.
[18] J.C. Jiang, E.I. Meletis, Microstructure of the nitride layer of AISI 316 stainless steel produced by intensified plasma assisted processing, J. Appl. Phys. 88(7) (2000) 4026-4031.
[19] E.I. Meletis, V. Singh, J.C. Jiang, On the single phase formed during low-temperature plasma nitriding of austenitic stainless steel, J. Mater. Sci. Lett. 21 (2002) 1171-1174.

[20] T. Christiansen, M.A.J. Somers, On the crystallographic structure of S-phase, Scripta Mater. 50 (2004) 35-37.
[21] T. Christiansen, M.A.J. Somers, Controlled dissolution of colossal quantities of nitrogen in stainless steel, Metall. Mater. Trans. A 37A (2006) 675-682.
[22] M.P. Fewell, J.M. Priest, High-order diffractometry of expanded austenite using synchrotron radiation, Surf. Coat. Technol. 202 (2008) 1802-1815.
[23] H. Dong, S-phase surface engineering of Fe-Cr, Co-Cr and Ni-Cr alloys, Int. Mater. Rev. 55(2) (2010) 65-98.
[24] B.K. Brink, K. Stahl, T.L. Christiansen, J. Oddershede, G. Winthiner, M.A.J. Somers, On the elusive crystal structure of expanded austenite, Scripta Mater. 131 (2017) 59-62.
[25] B.H. Kolster, Wear and corrosion resistant coatings on austenitic steels, VDI-Berichte (The Association of German Engineers) 506(107-113) (1983).
[26] R.H. van der Jagt, B.H. Kolster, M.W.H. Gillham, Anti-wear/corrosion treatment of finished austenitic stainless steel components: the Hardcor process, Mater. Des. 12 (1991) 41-46.
[27] O. Rey, P. Jacquot, Kolsterising: hardening of austenitic stainless steel, Surf. Eng. 18(6) (2002) 412-414.
[28] G.M. Michal, F. Ernst, A.H. Heuer, Carbon paraequilibrium in austenitic stainless steel, Metall. Trans. A 37A (2006) 1819-1824.
[29] F. Ernst, Y. Cao, G.M. Michal, A.H. Heuer, Carbide precipitation in austenitic stainless steel carburized at low temperature, Acta Mater. 55 (2007) 1895-1906.
[30] T.L. Christiansen, K. Stahl, B.K. Brink, M.A.J. Somers, On the carbon solubility in expanded austenite and formation of Hagg carbide in AISI 316 stainless steel, Steel Res. Int. 87(11) (2016) 1395-1405.
[31] X.Y. Li, S. Thaiwatthana, H. Dong, T. Bell, Thermal stability of carbon S phase in 316 stainless steel, Surf. Eng. 18 (2002) 448-452.
[32] T. Bell, Current status of supersaturated surface engineered S-phase materials, Key Eng. Mater. 373/374 (2008) 289.
[33] J.C. Stinville, P. Villechaise, C. Templier, J.P. Riviere, M. Drouet, Lattice rotation induced by plasma nitridng in a 316L polycrystalline stainless steel, Acta Mater. 58 (2010) 2814-2821.
[34] J.C. Stinville, C. Tromas, P. Villechaise, C. Templier, Anisotropy changes in hardness and indentation modulus induced by plasma nitriding of 316L polycrystalline stainless steel, Scripta Mater. 64 (2011) 37-40.
[35] J.C. Stinville, J. Cormier, C. Templier, P. Villechaise, Modeling of the lattice rotations induced by plasma nitriding of 316L polycrystalline stainless steel, Acta Mater. 83 (2015) 10-16.
[36] F.A.P. Fernandes, T.L. Christiansen, G. Winther, M.A.J. Somers, On the determination of stress profiles in expanded austenite by grazing incidence X-ray diffraction and successive layer removal, Acta Mater. 94 (2015) 271-280.
[37] K. Tong, F. Ye, H. Che, M.K. Lei, S. Miao, C. Zhang, High-density stacking faults in a supersaturated nitrided layer on austenitic stainless steel, J. Appl. Crystallogr. 49 (2016) 1967-1971.
[38] X.Y. Li, Y. Sun, Transmission electron microscopy study of S phase in low temperature plasma nitrided 316 stainless steel, in: T. Bell, K. Akamatsu (Eds.), Stainless Steel 2000: Thermochemical Surface Engineering of Stainless Steel, Maney Publishing, London, 2001.
[39] D. Stroz, M. Psoda, TEM studies of plasma nitrided austenitic stainless steel, J. Microsc. 237 (2010) 227-231.

[40] T.H. Lee, E. Shin, C.S. Oh, H.Y. Ha, S.J. Kim, Correlation between stacking fault energy and deformation microstructure in high-interstitial-alloyed austenitic steels, Acta Mater. 58 (2010) 3173-3186.
[41] R.E. Schramm, R.P. Reed, Stacking fault energies of seven commercial austenitic stainless steels, Metall. Trans. A 6A (1975) 1345.
[42] J. Talonen, H. Hanninen, Formation of shear bands and strain-induced martensite during plastic deformation of metastable austenitic stainless steels, Acta Mater. 55 (2007) 6108-6118.
[43] J.P. Riviere, M. Cahoreau, P. Meheust, Chemical bonding of nitrogen in low energy high flux implanted austenitic stainless steel, J. Appl. Phys. 91(10) (2002) 6361-6366.
[44] J. Oddershede, T.L. Christiansen, K. Stahl, M.A.J. Somers, Extended X-ray absorption fine structure investigation of nitrogen stabilized expanded austenite, Scripta Mater. 62 (2010) 290-293.
[45] A. Leyland, K.S. Fancey, A.S. James, A. Matthews, Enhanced plasma nitriding at low pressures: a comparative study of d.c. and r.f. techniques, Surf. Coat. Technol. 41 (1990) 295-304.
[46] L. Vitos, J.O. Nilsson, B. Johansson, Alloying effects on the stacking fault energy in austenitic stainless steels from first-principles theory, Acta Mater. 54 (2006) 3821-3826.
[47] J. Lu, L. Hultman, E. Holmstrom, K.H. Antonsson, M. Grehk, W. Li, L. Vitos, A. Golpayegani, Stacking fault energies in austenitic stainless steels, Acta Mater. 111 (2016) 39-46.
[48] V. Gavriljuk, Y. Petrov, B. Shanina, Effect of nitrogen on the electron structure and stacking fault energy in austenitic steels, Scripta Mater. 55 (2006) 537-540.
[49] L. Mosecker, A. Saeed-Akbari, Nitrogen in chromium-manganese stainless steels: a review on the evalution of stacking fault energy by computational thermodynamics, Sci. Technol. Adv. Mater. 14 (2013) 033001.
[50] J. Buhagiar, X. Li, H. Dong, Formation and microstructural characterisation of S-phase layers in Ni-free austenitic stainless steels by low-temperature plasma surface alloying, Surf. Coat. Technol. 204(3) (2009) 330-335.
[51] J. Dudala, J. Gilewicz-Wolter, Z. Stegowski, Simultaneous measurement of Cr, Mn and Fe diffusion in chromium-manganese steels, Nukleonika 50(2) (2005) 67-71.
[52] T. Christiansen, M.A.J. Somers, Decomposition kinetics of expanded austenite with high nitrogen contents, Z. Metallkd. 97(1) (2006) 79-88.
[53] G.A. Collins, R. Hutchings, K.T. Short, J. Tendys, X. Li, M. Sammandi, Nitriding of austenitic stainless steel by plasma immersion ion implantation, Surf. Coat. Technol. 74-75 (1995) 417-424.
[54] H.A. Wriedt, N.A. Gokcen, R.H. Nafziger, The Fe-N (iron-nitrogen) system, Bull. Alloy Phase Diagr. 8 (1987) 355.
[55] C.M. Zener, Elasticity and anelasticity of metals, University of Chicago Press, Chicago, 1948.
[56] K. Morii, H. Mecking, Y. Nakayama, Development of shear bands in F.C.C. single crystals, Acta Metall. 33(3) (1985) 379-386.
[57] A. Korbel, J.D. Embury, M. Hatherly, P.L. Martin, H.W. Erbsloh, Microstructural aspects of strain localization in Al-Mg alloys, Acta Metall. 34(10) (1986) 1999-2009.
[58] P. Wagner, O. Engler, K. Lucke, Texture development in Al-3% Mg Influenced by shear bands, Textures Microstruct. 14-18 (1991) 927-932.
[59] S. Allain, J.P. Chateau, O. Bouaziz, S. Migot, N. Guelton, Correlation between the calculated stacking fault energy and the plasticity mechnisms in Fe-Mn-C alloys, Mater. Sci. Eng., A 387-389 (2004) 158-162.

[60] Y. Cao, F. Ernst, G.M. Michal, Colossal carbon supersaturation in austenitic stainless steels carburized at low temperature, Acta Mater. 51 (2003) 4171-4181.
[61] S. Collins, P. Williams, Low-temperature colossal supersaturation, Advanced Materials and Process, ASM International, 2006, pp. 32-33.
[62] G. Taylor, Plastic strain in metals, J. Inst. Met. 62 (1938) 307-324.
[63] J. Bishop, R. Hill, A theory of the plastic distortion of a polycrystalline aggregate under combined stresses, Philos. Mag. 42 (1951) 1298-1307.
[64] J. Bishop, A theory of the tensile and compressive textures of face-centred cubic metals, J. Mech. Phys. Solids 3 (1955) 130-142.
[65] B. Clausen, T. Lorentzen, T. Leffers, Self-consistent modeling of the plastic deformation of F.C.C. polycrystals and its implications for diffraction measurements of internal stresses Acta Mater. 46(9) (1998) 3087-3098.
[66] T. Christiansen, K.L. Dahm, M.A.J. Somers, New stainless steel alloys for low temperature surface hardening, BHM Berg- und Hüttenmännische Monatshefte 160(9) (2015) 406-412.

A low stacking fault energy (SFE) ASS (i.e. Fe-17Cr-20Mn-0.5N, in wt.%) after nitriding at 400-450°C, Beam//<110>γ_N

Structure evolution with increasing treatment time and/or temperature

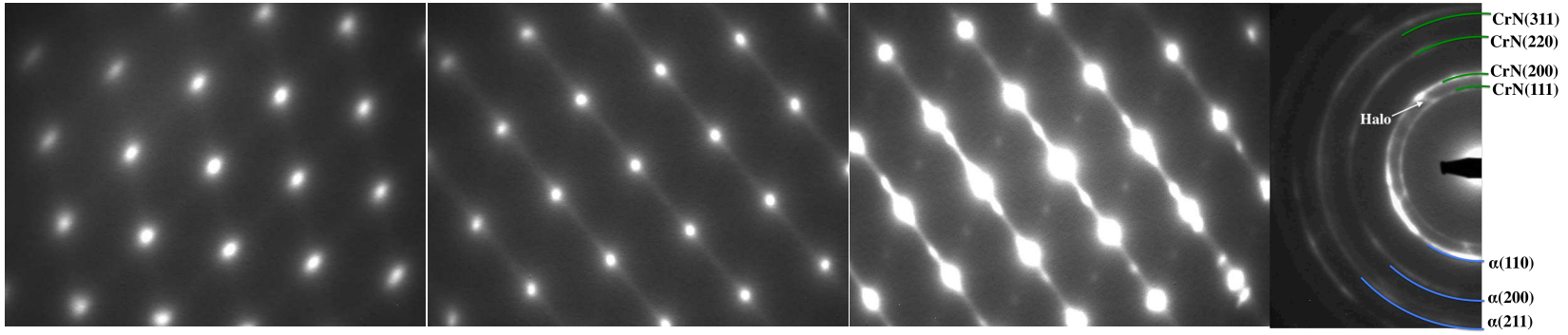

FCC cubic structure | … + SF generation | … + ε-martensite formation, and ordered nitrogen occupation | After phase decomposition

A high SFE ASS (i.e. Fe-19Cr-35Ni, in wt.%) after nitriding at 400-450°C, Beam//<110>γ_N

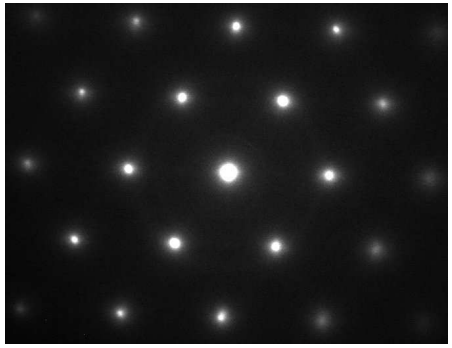

FCC structure with low SF density (or SF-free), and random nitrogen occupation in FCC lattice

Structure evolution with increasing treatment time and/or temperature

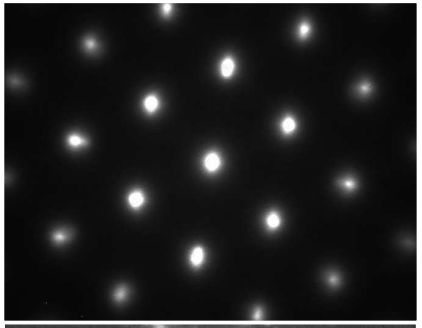

Sluggish phase decomposition inside γ_N grain

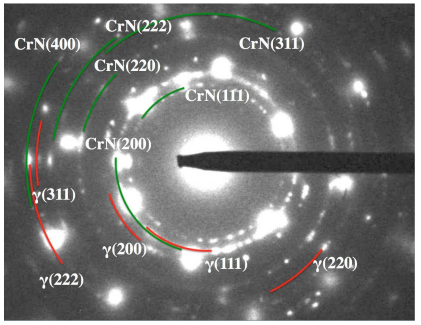

Polycrystalline precipitates at grain boundary

Tables

Table 1. Material compositions, in wt.%

Material	ASTM	Code	Fe	Cr	Ni	Mn	N	Others
AISI 304[A]	ASTM A240	304	Bal.	18.2	8.1	1.7	/	0.3 Si
Staballoy AG17®[B]	/	AG17	Bal.	17.4	0.8	18.9	0.47	0.6 Co, 0.3 Si
RA 330®[C]	ASTM B536-07	330	Bal.	18.5	34.9	1.4	0.01	0.16 Al, 0.14 Ti, 0.11 Cu, 1.2 Si, 0.05 C

[A]Composition of AISI 304 was based on EDX analysis; [B]Composition of Staballoy AG17® was based on EDX analysis (with nitrogen content specifically determined via chemical analysis performed by Sheffield Assay Office); [C]Composition of RA 330® was based on chemical analysis from original material supplier (i.e. ATI Allegheny Ludlum Corporation), with the contents of major alloying elements (i.e. Cr, Ni, Mn and Si) confirmed via EDX analysis

Table 2. Surface nitrogen contents and layer depths

TPN Treatment	Surface at.% Nitrogen		Layer depths, µm	
	Alloy AG17	Alloy 330	Alloy AG17	Alloy 330
400°C 4hrs	27.8 ± 0.2	23.1 ± 0.6	1.8 ± 0.1	2.1 ± 0.1
400°C 20hrs	34.4 ± 0.6	24.0 ± 0.8	5.3 ± 0.1	4.3 ± 0.1
425°C 4hrs	29.6 ± 0.4	24.1 ± 0.5	2.8 ± 0.1	3.1 ± 0.1
425°C 20hrs	34.3 ± 0.7	25.7 ± 0.9	12.0 ± 0.3	10.4 ± 0.3
450°C 4hrs	26.5 ± 0.5	22.6 ± 0.8	3.5 ± 0.1	3.4 ± 0.1
450°C 20hrs	29.2 ± 0.3	25.1 ± 0.5	18.5 ± 0.4	13.8 ± 0.2

*The data presented (mean value ± 95% confidence interval) are derived from measurements described in experimental procedure

Figures

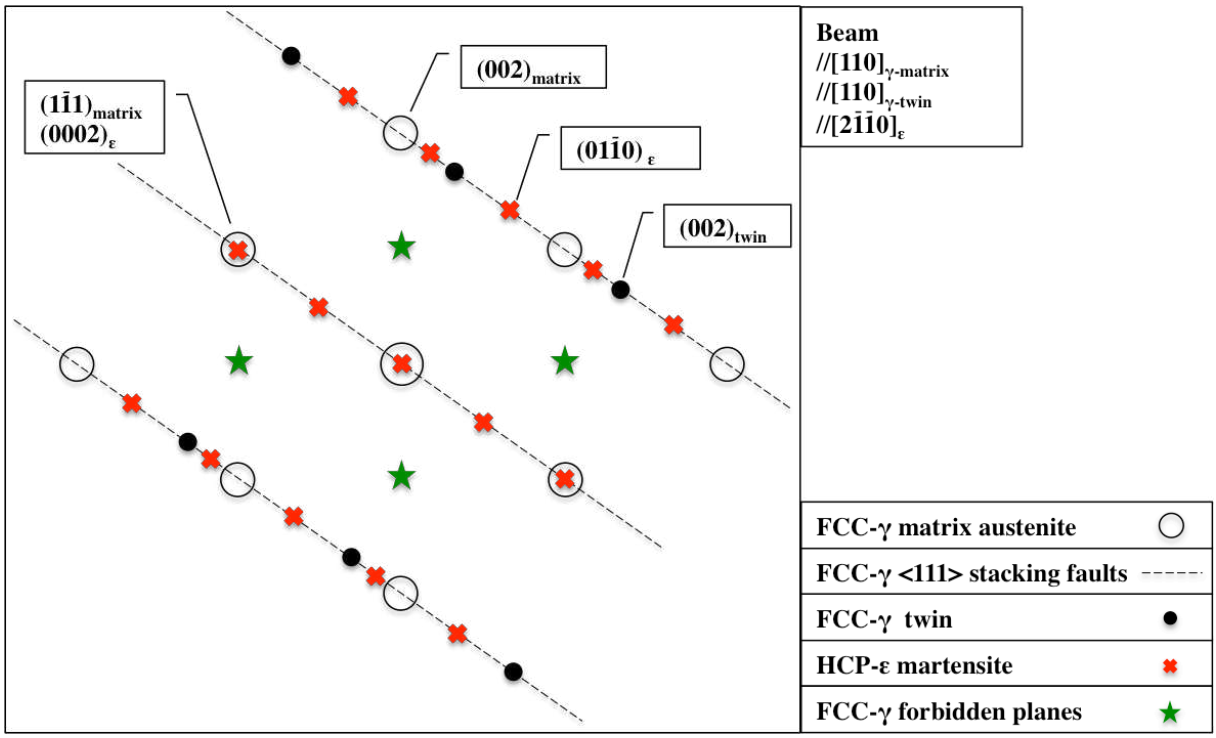

Fig. 1 Illustration of electron diffraction features observable for high SF density regions in γ_N that was hinted at in Ref. **[18, 19, 37-39]**. Apart from the forbidden reflections of FCC planes, the other features (i.e. <111> SFs, twinning and local HCP arrangement in γ_N) are consistent with those of mechanically deformed ASS, such as in Ref. **[40]**

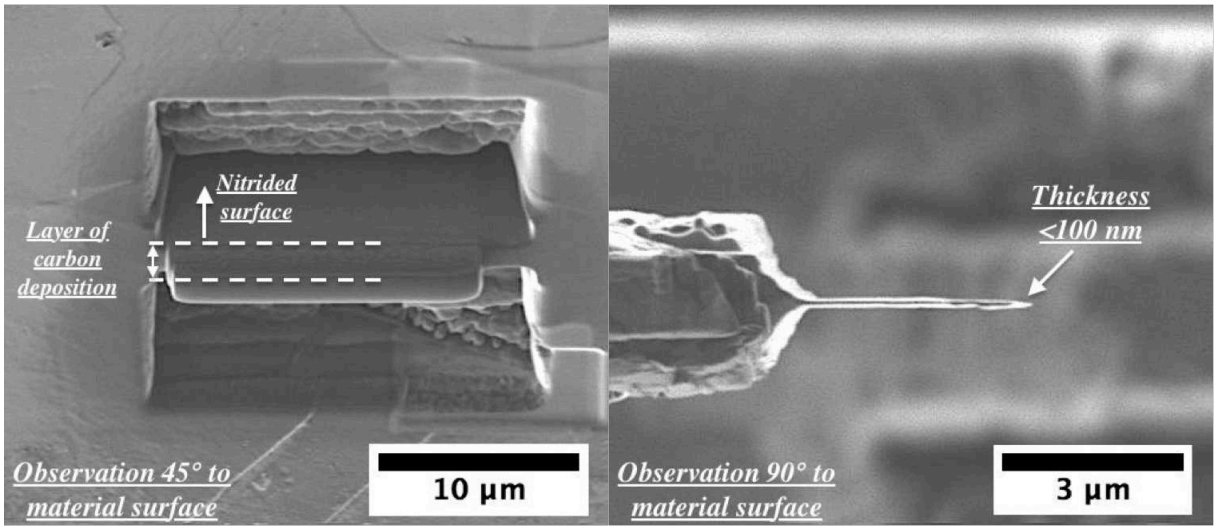

Fig. 2 Ion beam images illustrating focused ion beam (FIB) method for TEM thin foil preparation

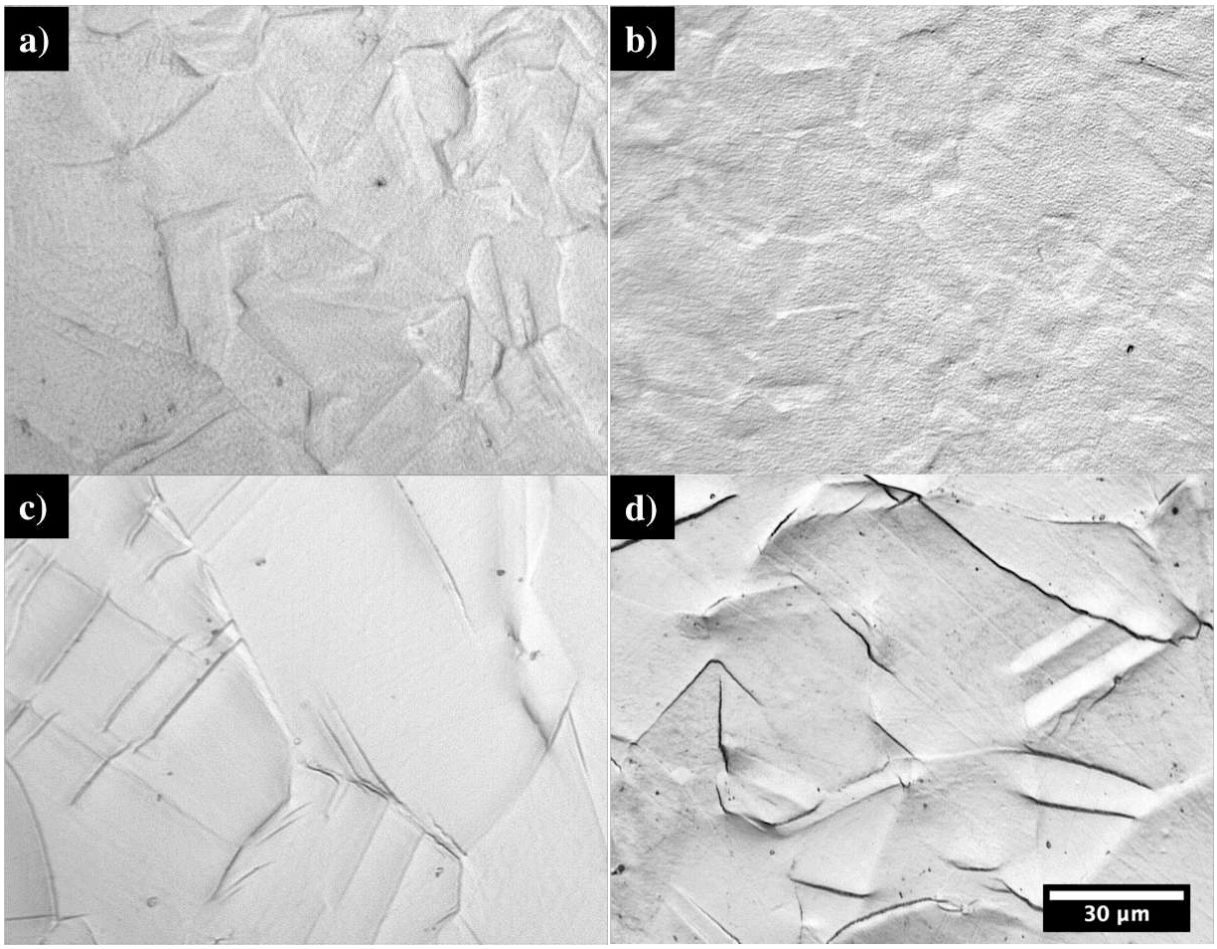

Fig. 3 Optical images of plasma nitrided surfaces. Staballoy AG17® after plasma nitriding a) at 400°C for 20hrs, b) at 450°C for 20hrs; RA 330® after plasma nitriding c) at 400°C for 20hrs, d) at 450°C for 20hrs

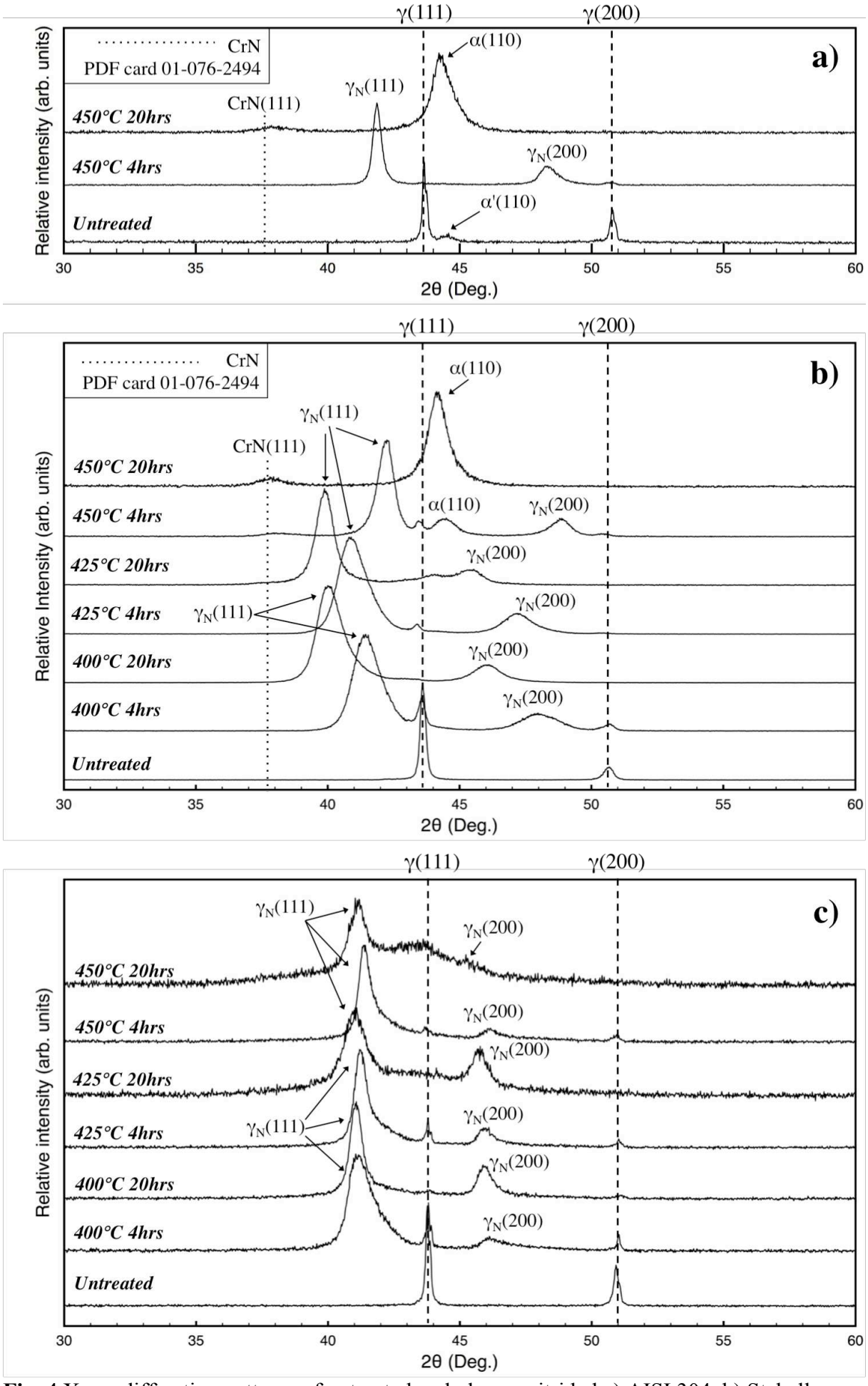

Fig. 4 X-ray diffraction patterns of untreated and plasma nitrided a) AISI 304, b) Staballoy AG17®, and c) RA 330® (γ-austenite, γ_N-nitrogen expanded austenite, α′-mechanically induced martensite, α-ferrite, CrN-Chromium nitride)

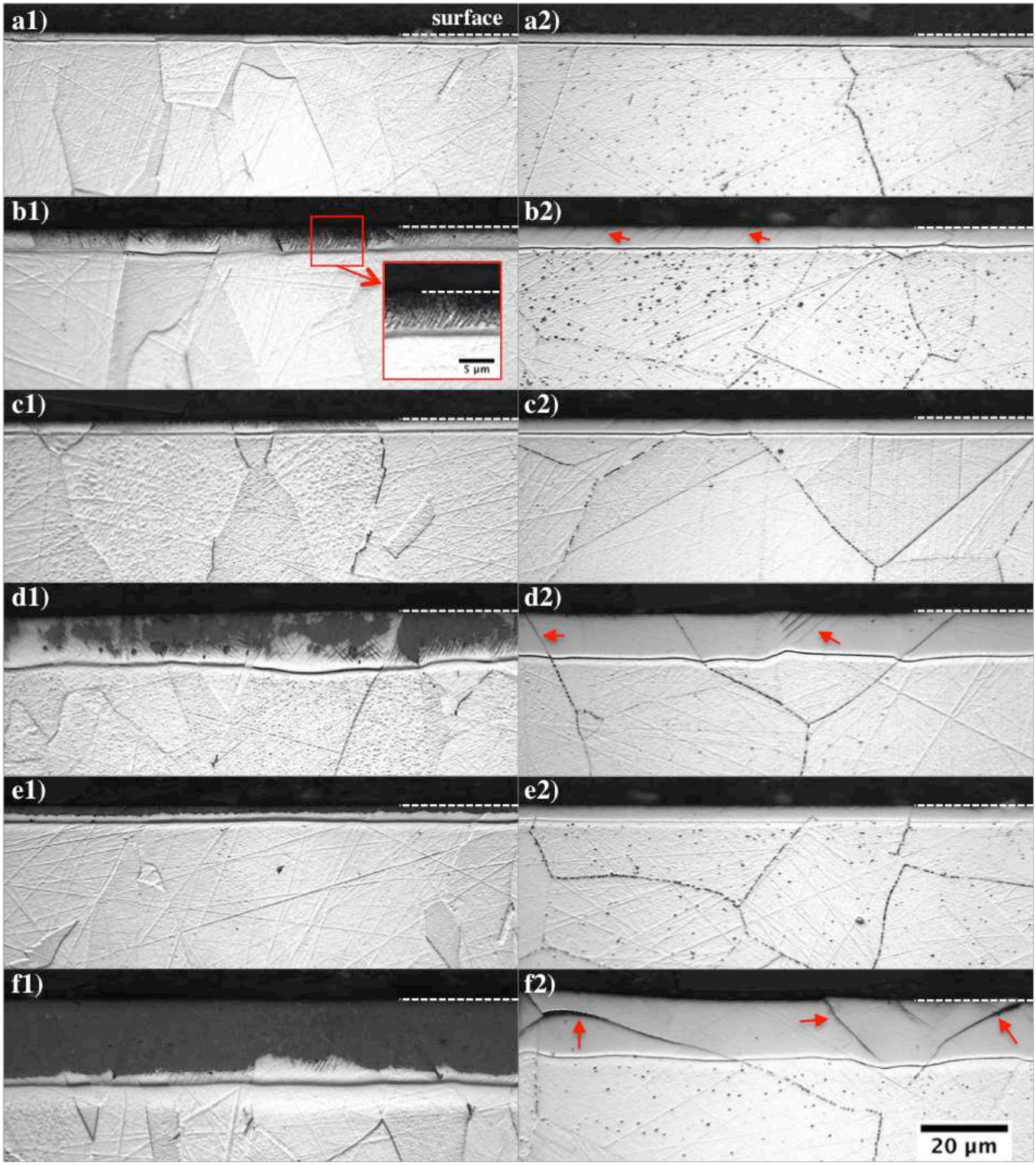

Fig. 5 Optical images of alloy AG17 (left column) and 330 (right column) after TPN a) at 400°C for 4hrs, b) at 400°C for 20hrs, c) at 425°C for 4hrs, d) at 425°C for 20hrs, e) at 450°C for 4hrs, f) at 450°C for 20hrs.

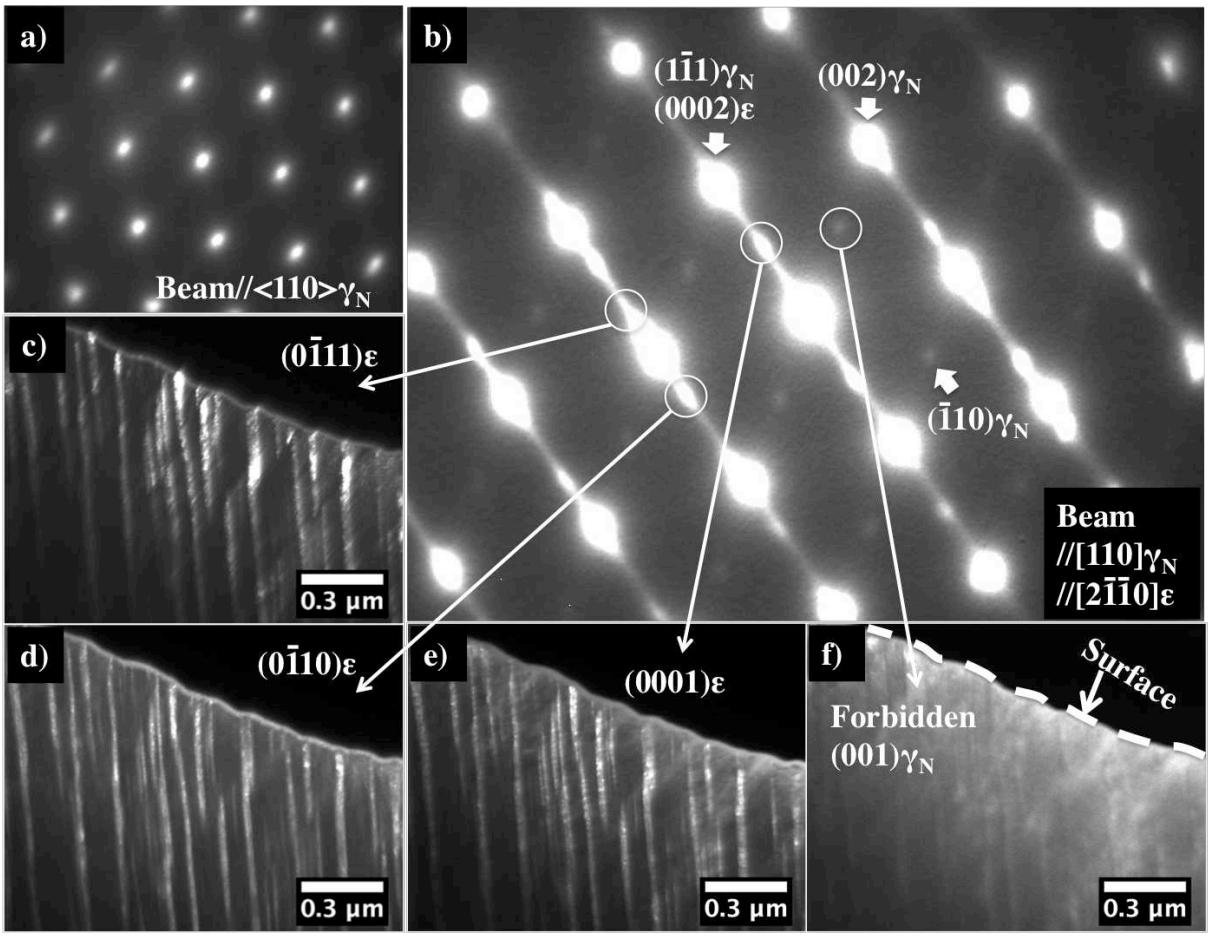

Fig. 6 EDPs of the near surface region of Staballoy AG17® after plasma nitriding a) at 400°C for 4hrs, b) at 400°C for 20hrs, and c-f) corresponding DF-TEM images of the near surface region of Staballoy AG17® after nitriding at 400°C for 20hrs (DF-TEM images were constructed by different diffraction electrons as indicated in figure)

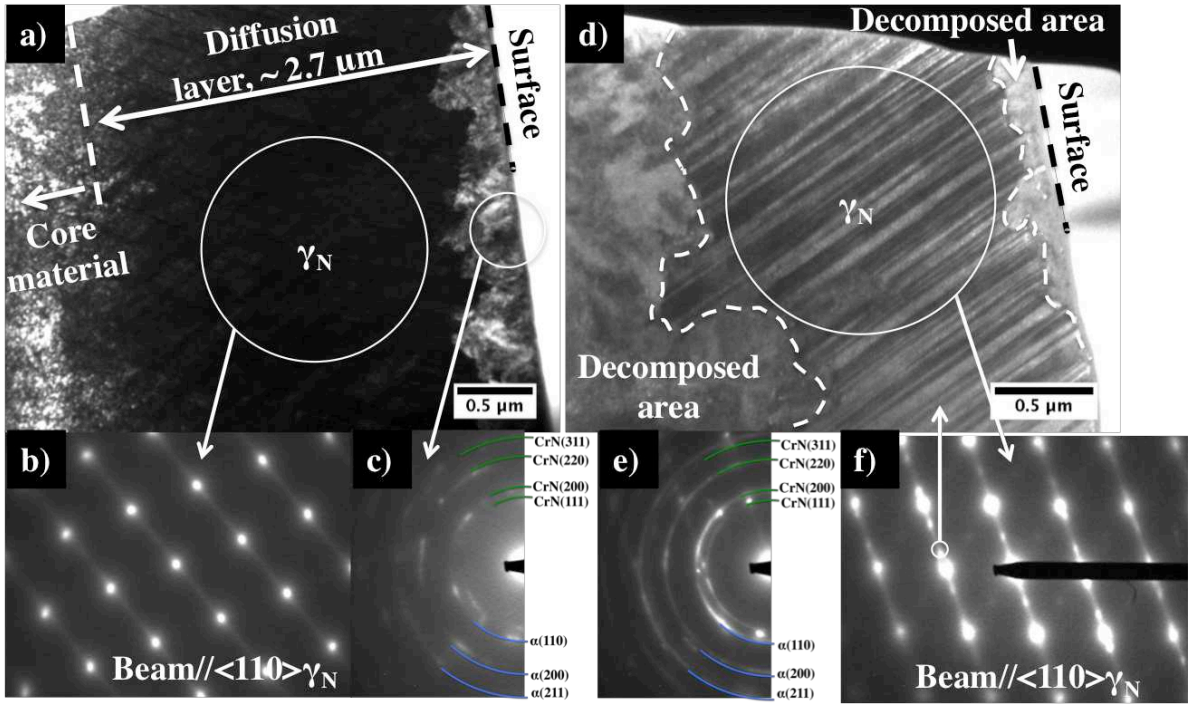

Fig. 7 TEM images, EDPs of Staballoy AG17® after plasma nitriding at 425°C for 4hrs and 20hrs. a-c) BF-TEM image of 425°C 4hrs nitrided AG17 and corresponding selected area EDPs, d) DF-TEM image of 425°C 20hrs nitrided AG17 (constructed by diffraction electrons as indicated in figure f), e) EDP of the entire prepared TEM sample of 425°C 20hrs nitrided AG17, f) Selected area EDP of γ_N in image d

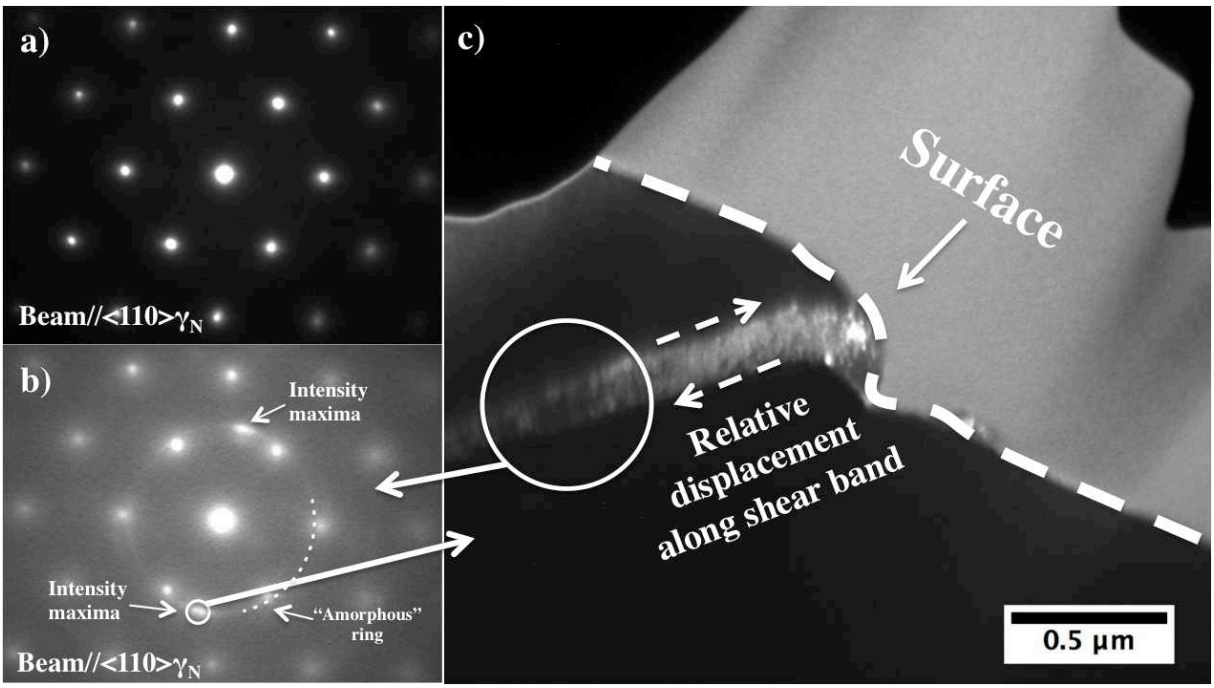

Fig. 8 a) EDP of expanded austenite generated on RA 330® after nitriding at 400°C 20hrs, b) selective area EDP of localised lattice distortion from region shown in image c, c) DF-TEM image showing a shear band, DF-TEM image was constructed by diffraction electrons as indicated in image

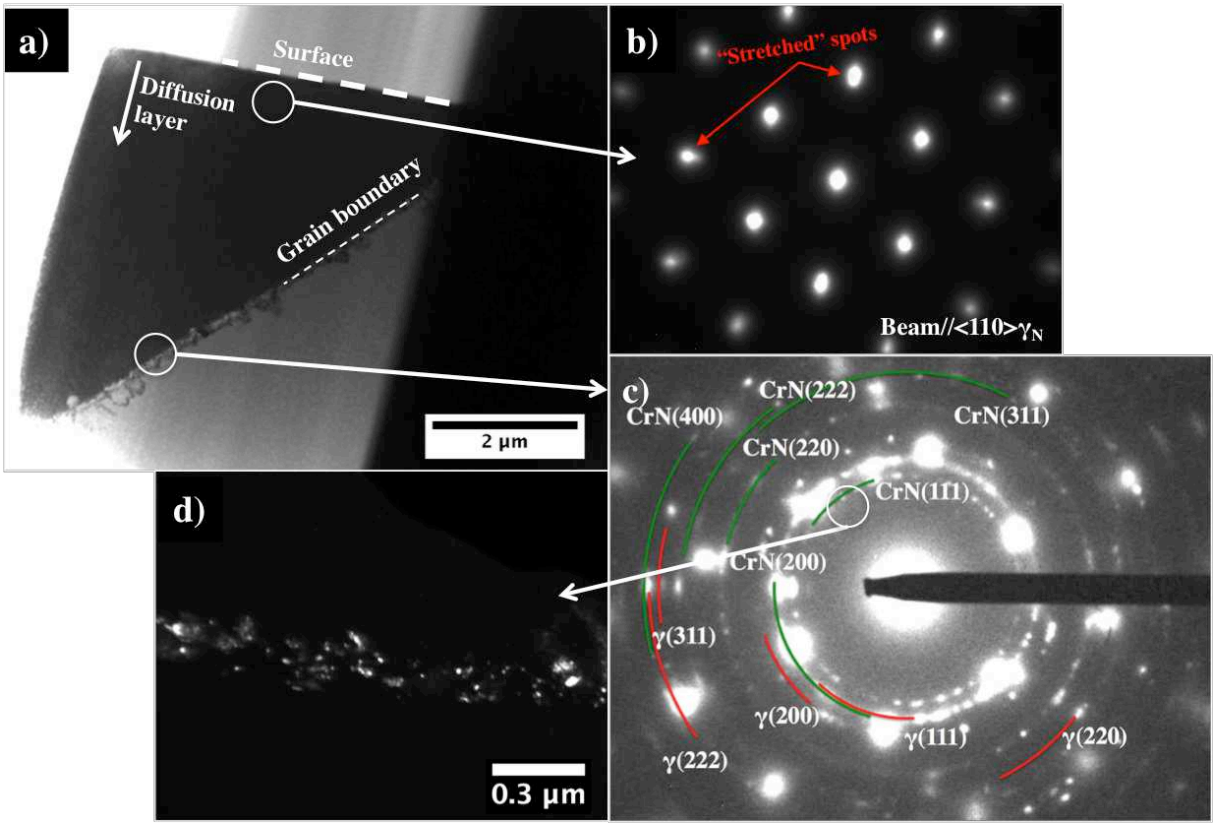

Fig. 9 a) low magnification BF-TEM image of the 450°C 20hrs plasma nitrided RA 330®, b-c) corresponding selected area EDPs, d) DF-TEM image of the grain boundary region, DF-TEM image was constructed by CrN(111) diffraction electrons as indicated in figure c

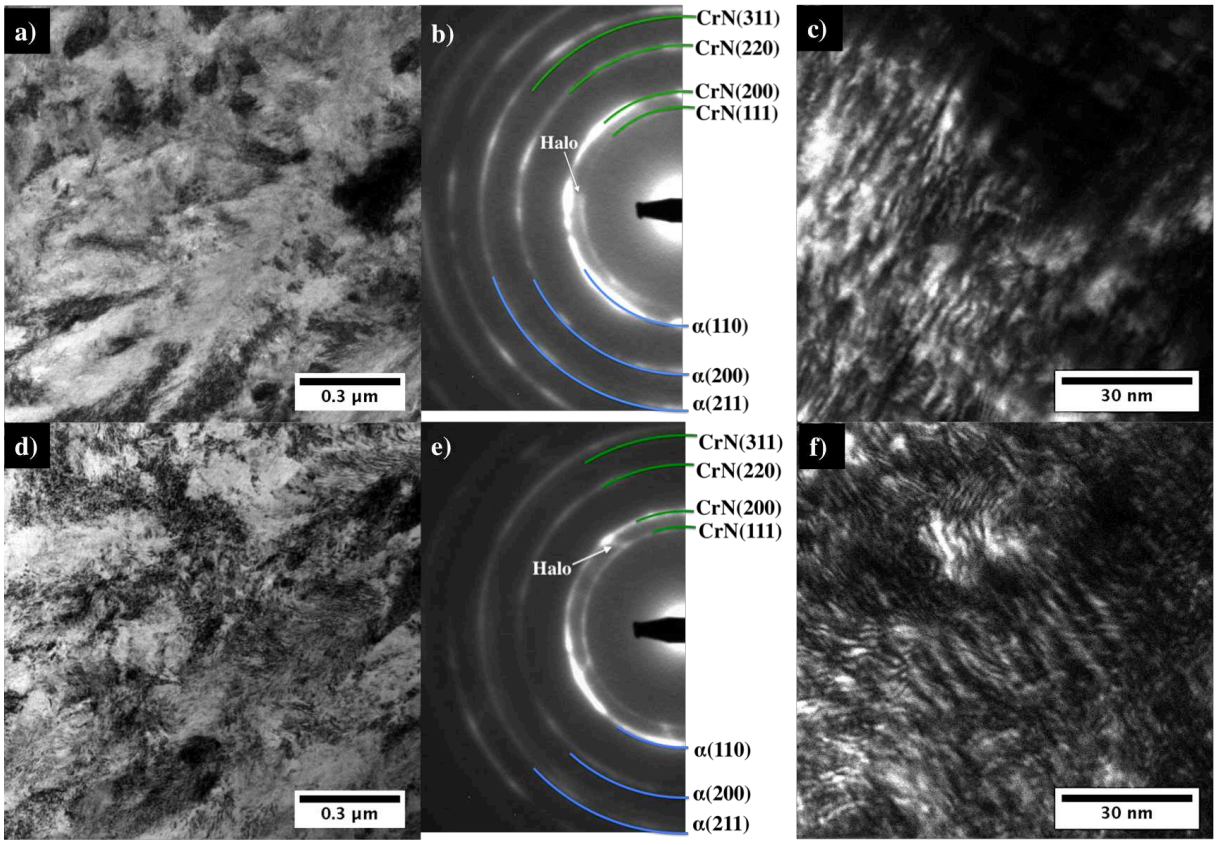

Fig. 10 BF-TEM images, EDPs, and DF-TEM images of 450°C and 20hrs plasma nitrided AISI 304 (a, b, c, respectively) and Staballoy AG17® (d, e, f, respectively). DF-TEM images were constructed by CrN(111) diffraction electrons

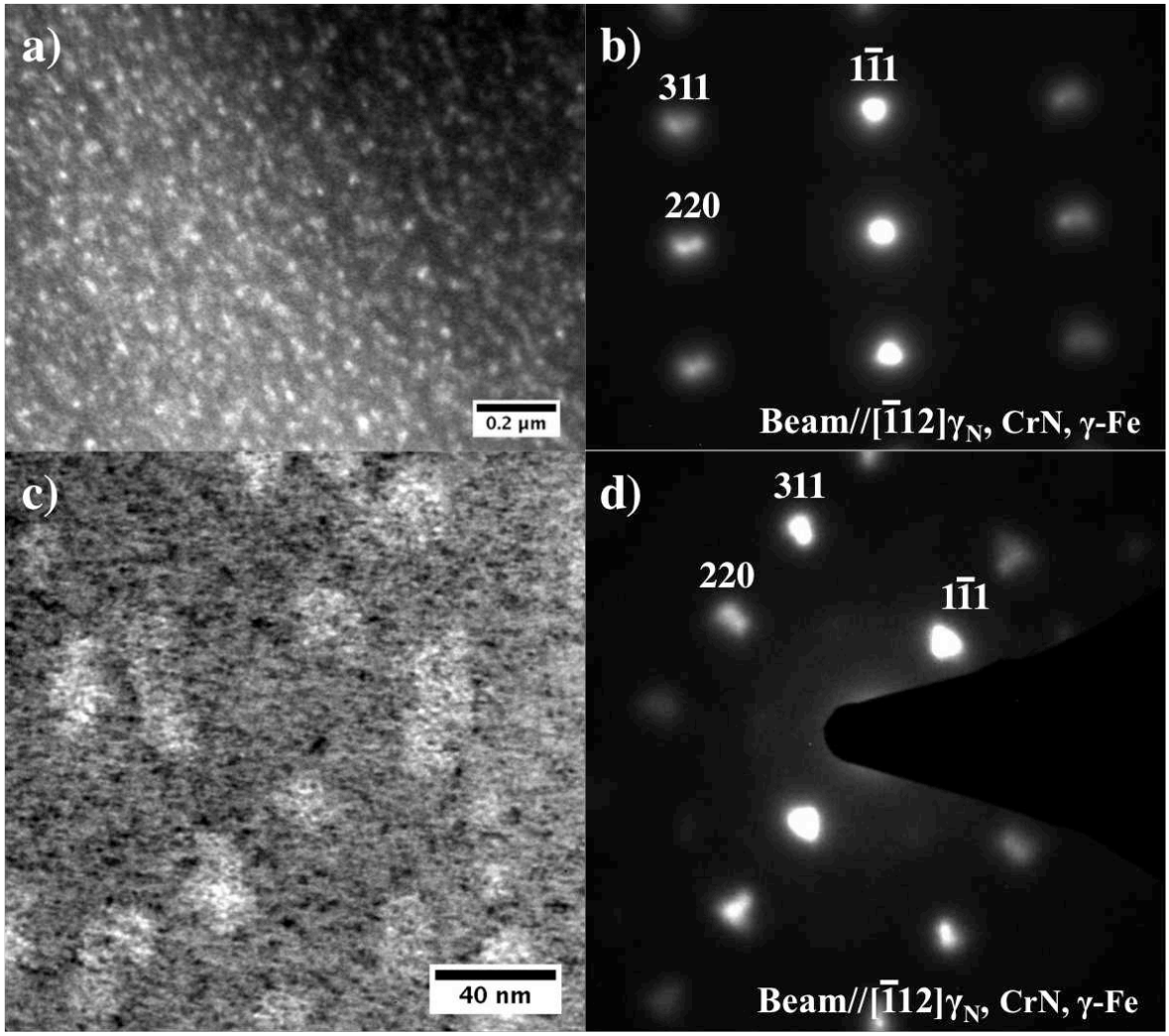

Fig. 11 BF-TEM images and EDPs of the 450°C 20hrs plasma nitrided RA 330® extracted via Philips EM420 (a, b, respectively) and FEI Tecnai T20 (c, d, respectively)